
UNIVERSITY OF CRETE - DEPARTMENT OF
PHYSICS

INSTITUTE OF ELECTRONIC STRUCTURE AND
LASER-FOUNDATION FOR RESEARCH AND
TECHNOLOGY

Master Thesis

Laser beam Shaping for Multi-photon polymerization

By

Maria Manousidaki

Academic advisor: Prof. Costas Fotakis

Supervisors: Prof. D. G. Papazoglou

Dr. Maria Farsari

Prof. Stelios Tzortzakis

October 2014

ABSTRACT

It is the past few years that a new type of non-diffracting beams, finite-energy Airy beams, was first introduced. The Airy wavepacket features the unique property to freely accelerate, following a parabolic trajectory, while keeping a constant central lobe diameter over propagation.

Cylindrically symmetric Airy beams or the so-called ring-Airy beams, were recently shown. These beams can abruptly autofocus, along their propagation, delivering high intensity contrast at the focus position. These non-diffractive beams have attracted a great deal of interest due to their remarkable characteristics. It is quite interesting the fact that such beams present long working distances, tight focusing and small focal volumes, while nonlinear propagation effects can be very exciting.

In the following Master Thesis, we demonstrate experimentally generated ring-Airy beams using a Fourier Transform (FT) approach and a simple method to spatially control their autofocus position. The radially symmetric Airy distribution can be generated using the FT of a properly modulated input wave. In particular, a Gaussian beam is modulated by a cubic phase, using a phase reflecting only spatial light modulator (SLM), and its FT will give the ring-Airy distribution. By modulating the characteristics of such beams at the plane of generation, we prove that we control the working distance of these beams and the focal voxel dimensions and shape. We show that the generated ring Airy beams have a high aspect ratio focal voxel that can be positioned at different working distances keeping almost invariant its dimensions and shape. Moreover, we report on parametric results of such ring Airy beams and demonstrate that the working distance control of Bessel beam is also possible.

These notable abilities of ring Airy beams make them ideal candidates for direct laser writing by Multi-photon polymerization. Multi-photon polymerization (MPP) of photosensitive materials allows one to fabricate complicated three-dimensional (3D) microstructures. When a fs infrared laser is tightly focused into the volume of a photosensitive resin, femtosecond laser pulses can cause MPP and produce structures with sub-micrometers resolution and lower. The controllable, long working distance and the high aspect ratio focal volume, surpass the restrictions set to the overall height of a 3D structure when using Gaussian beams and small working distance, high NA objective lenses; and long-range MPP can be achieved.

Therefore, we present 3D structures made using ring-Airy beams that were set to autofocus inside the volume of a photoresist while the sample was moved only on the x-y plane.

In conclusion, tunable ring Airy beams are employed for direct laser writing using Multi-photon polymerization. These beams present high aspect ratio focal voxels which can be shifted at different working distances while remains almost invariant, an attribute that makes these beams ideal candidates for long range Multi-photon polymerization. Examples of fabricated 3D microstructures are presented as well as theoretical calculations and comparison with Bessel beams.

ACKNOWLEDGMENTS

Thanking those who have helped and guided me during my graduate studies here in University of Crete and the Institute of Electronic structure and Laser of Foundation for Research and Technology (FORTH), is my duty and pleasure.

I would like to thank *Professor C. Fotakis*, President of FORTH, for being the academic advisor of this Master thesis. His valuable support was more than important for the completion of this research.

My deepest gratitude is to my supervisors: I am grateful to *Professor Stelios Tzortzakis* for giving me the opportunity to join his group (Nonlinear laser Interactions and Sources research group (UNIS)) and for all his guidance and support during all stages of my master studies. His creativity, his passion for research and educating his students are some of the qualities that a graduate student would hope finding in an advisor. Also, I will be always indebted to the co-supervisor of my Master thesis, *Professor D. G. Papazoglou* for his deep involvement in every aspect of research, his unpretentious way of exploring things, for his patience, motivation, enthusiasm, for the long and helpful discussions, the advice and the continuous guidance.

Next, I would like to thank *Dr. Maria Farsari* for being the advisor of my graduate studies, for giving me the opportunity to be member of the Non-Linear lithography group (NNL) in IESL-FORTH since 2011, for all the support, for the valuable discussions and suggestions, and most importantly I am grateful to her because this Thesis would not have been possible without her contribution.

Also, I need to thank all the members of the two research groups that I involved with and especially Michalis Loulakis from UNIS group and Alexandros Selimis from NNL group for all their help and advice during my research studies.

Finally, none of this would have been possible without the love, support and patience of my family.

TABLE OF CONTENTS

Abstract.....	1-2
Acknowledgments	3
Contents	4-5
INTRODUCTION	6-7
PART I - Theoretical background.....	8
CHAPTER ONE - Airy Beams & Abruptly autofocusing beams	9-17
1.1 Introduction	9
1.2 Infinite and Truncated-Energy Airy beams	9-11
1.3 Experimental observation of 1D nad 2D Finite Airy beams	11-13
1.4 Radially Symmenttic Autofocusing beams	13-16
References	17
CHAPTER TWO - Laser beam Shaping	18-31
2.1 Introduction	18
2.2 General shaping problem	18-20
2.3 Fourier Transform approach.....	20-25
2.4 Fourier Transform in 4f Optical correlator.....	26
2.5 Spatial Light modulator	27-30
References	31
CHAPTER THREE - Multi-photon Polymerization by Direct Laser writing.....	32-40
3.1 Introduction	32
3.2 Two photon absorption	32-33
3.3 Photo-polymerization.....	33-36

3.4 Materials for Laser Polymerization.....	36-38
References	39-40
Part II- Experimental Demonstration.....	411
CHAPTER FOUR- Tunable ring-Airy beams generation and Control dynamics	42-54
4.1 Introduction	42
4.2 Expeimental Demonstration	42- 43
4.3 Ring-Airy beam Manoipulation- Working distance Control.....	43-47
4.4 The ring-Airy focal Voxel - Dimensions and Shape.....	47-48
4.5 Bessel beam and Comparison with ring-Airy beam.....	48-53
References	54
CHAPTER FIVE- Multi-photon Polymerizting using Abruptly autofocusing beams	55-62
5.1 Introduction	55-56
5.2 Set-up for MPP by ring- Airy beams	56-57
5.3 Photosensitive Materials for MPP by ring-Airy beams.....	57-58
5.4 3D structures fabricated by ring-iry beams & MPP.....	59-61
References	62
PART III	CONCLUSIONS.....63

INTRODUCTION

An important consideration in optical systems is the dynamics of the optical beam that passes through that system to deliver energy, power or information in an appropriate and efficient manner. Since the advent of the laser, many applications have required shaping the beam profile. Several of the primary applications involve material processing, medical applications, lithography semiconductor manufacture and optical data processing.

Beam shaping is the process of redistributing the irradiance and phase of a beam. The beam's shape is defined by the irradiance distribution. The phase of the shaped beam is a major factor in determining the propagation properties of the beam profile. Therefore, there is a continuous research on phase modulation procedures and optical methods that can redistribute a beam's profile, reshaping its wavefront and modifying the propagation dynamics of this beam.

There are various examples of shaped laser beams studied in literature. Some of them are the Bessel beams, Top hat beams, Vortex beams etc. In this Master Thesis, we are focusing on Airy beams and specifically on radially symmetric Airy beam. Airy beams were firstly introduced by Berry and Balazs (1979). The Airy wavepacket features the unique property to freely accelerate even in the absence of any external potential while it remains non-diffracting. In addition the transverse acceleration of the Airy beam causes the beam to follow a parabolic trajectory, while keeping a constant central lobe diameter. This exotic propagation dynamics are caused by a strong spatial cubic phase which is imprinted on the beam profile.

Radially symmetric Airy beams or ring-Airy beams are a new type of non-diffracting beam which was introduced the past few years. This kind of beams tend to abruptly autofocus, delivering high intensity contrast at the focal position. The maximum intensity of such a radial wave remains almost constant during propagation while it suddenly increases by orders of magnitude right before its focal point.

Here, we demonstrate the experimental generation of ring-Airy beams using a Fourier Transform (FT) approach. In particular, the radially symmetric Airy distribution can be generated using the FT of a properly modulated input wave. A phase reflecting only spatial light modulator (SLM) is employed for the phase modulation of a Gaussian beam which is then properly Fourier transformed. In the next step we are aiming to control the propagation dynamics of these beams. Therefore, we present a simple method to spatially control their autofocus position. Another important issue was the focal voxel manipulation. We show that these beams have a high aspect ratio focal voxel that can be positioned at different working distances keeping almost invariant its dimensions and shape.

The remarkable abilities of ring Airy beams that we discover here introduce them as ideal candidates for direct laser writing by multiphoton polymerization. The controllable, long working distance and the high aspect ratio focal volume, surpass the restrictions set to the overall height of a 3D structure when using Gaussian beams and small working distance, high NA objective lenses. We present 3D structures made using ring-Airy beams that were set to autofocus inside the volume of a photoresist while the sample was moved only on the x-y plane. Such structures could be used on many applications such as biological or tissue engineering.

Bessel beams are studied too. We report on the approach of controlling the working distance of a Bessel beam during propagation. In comparison with Bessel beams, ring-Airy beams present a more effective control of the focal voxel dimensions and shape during their propagation.

For the easiest study of this Master Thesis, a description of the following chapters is reported. The thesis is composed by three main parts: the theoretical part which includes the basic theoretical background (Part I), the experimental part which explains the experimental procedures (Part II) and the third part containing general conclusions (Part III). In Chapter One the basic theoretical knowledge about Airy beams and abruptly autofocusing beams is mentioned while in Chapter Two the idea of beam shaping is explained. In Chapter Three the Multi-Photon Polymerization by Direct Laser Writing technique is presented. The experimental demonstration of the tunable Ring-Airy beams, their generation and the control of their dynamics are described in Chapter Four. In the end, the Tailored Multiphoton Polymerization using abruptly autofocusing beams is showed in Chapter Five.

PART I - THEORETICAL BACKGROUND

1.1 Introduction

It is the past few years that a new type of non-diffracting beams, finite-energy Airy beams, was first introduced. These beams have attracted a great deal of interest due to their unique properties, like their self-acceleration feature [1, 2]. In 1979, Berry and Balazs theoretically demonstrate that in the field of quantum mechanics the spatial electric field profile of these beams, which is described by the Airy function, can exhibit the only non-spreading one-dimensional (1D) wave packet solution of the Schrodinger equation describing a free particle [3]. They also showed that the Airy wavepacket features the unique property to freely accelerate even in the absence of any external potential. In addition the transverse acceleration of the Airy beam causes the beam to follow a parabolic trajectory [4], while keeping a constant central lobe diameter. This exotic propagation dynamics are caused by a strong spatial cubic phase which is imprinted on the beam profile.

For the past few years, notable research work has been done to the study of Airy beams, from theoretical predictions to experimental observations, while many aspects of applications have been proposed [5-7]. In accordance to this research, the radially symmetric Airy beams were proposed [8]. These beams tend to autofocus in an abrupt fashion. Their maximum intensity radial profile remains almost invariant during propagation while it suddenly increases by orders of magnitude right before its focal point.

In this chapter, an overview on generation and linear control of Airy beams will be provided. Moreover, the radially symmetric Airy beams will be introduced and their characteristic properties will be discussed.

1.2 Infinite and Truncated-Energy Airy Beams

Let's consider the paraxial equation of diffraction that governs the propagation dynamics of the electric field envelope φ :

$$i \frac{\partial \varphi}{\partial \xi} + \frac{1}{2} \frac{\partial^2 \varphi}{\partial s^2} = 0 \quad (1.1)$$

In (1.1), $s = x/x_0$ represents a dimensionless transverse coordinate, x_0 is an arbitrary transverse scale, $x = z/kx_0^2$ is a normalized propagation distance and $k = 2\pi n/l_0$ is the wave number of the optical wave. As Berry and Balazs first shown in ref.1, the infinite-energy Airy nondispersive solution of eq. 1.1 is given by

$$\varphi(s, \xi) = Ai \left[s - \left(\frac{\xi}{2} \right)^2 \right] \exp \left(is \frac{\xi}{2} - \frac{i \xi^2}{12} \right) \quad (1.2)$$

Setting $\xi=0$, eq. 1.2 becomes $\varphi(s, 0) = Ai(s)$ showing that the intensity profile of this wave propagating over ξ will remain invariant while it experiences a constant transverse acceleration. Also, the term $(\xi/2)^2$ in (1.2) describes that the beams follows a ballistic trajectory.

However, any infinite-energy solution would not be possible in practice. For this reason, the truncated Airy beams must be introduced. To do that, we assume an exponential function:

$$\varphi(s, 0) = Ai(s) \exp(\alpha s) \quad (1.3)$$

The decay factor $\alpha > 0$ possesses the physical realization of such beams. Figure 1.1a depicts the field profile of such a finite-energy 1D Airy beam at $\xi=0$, whereas Fig. 1.1b plots its corresponding intensity [1].

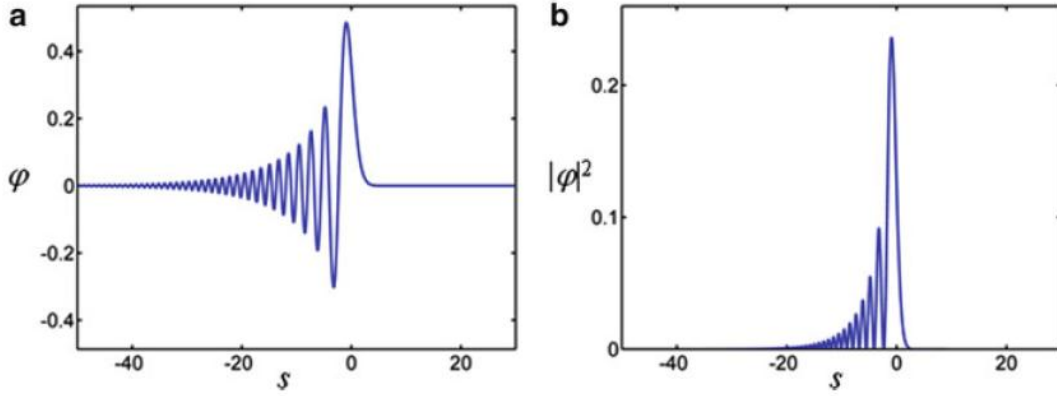


Figure 1.1| Normalized field profile (a) and intensity profile (b) of a finite-energy Airy beam when $\alpha=0.1$. [1]

According to Ref. 1, by directly solving Eq. 1.1 under the initial conditions of Eq. 1.3, we find that the Airy beam evolves according to:

$$\varphi(s, \xi) = Ai \left[s - \left(\frac{\xi}{2} \right)^2 + i\alpha\xi \right] \exp \left(\alpha s - \left(\alpha \frac{\xi^2}{2} \right) - i \left(\frac{\xi^3}{12} \right) + i \left(\alpha^2 \frac{\xi}{2} \right) + i \left(s \frac{\xi}{2} \right) \right) \quad (1.4)$$

The Airy wavepacket tends to freely accelerate. This exotic behavior is rather peculiar by the fact that it may occur in free space. This characteristic is reflected in the term $s - (\xi/2)^2$

appearing in the Airy function (Eq. 1.4). The acceleration dynamics are clearly observed in Figure 1.2 where the parabolic trajectory of the beam can be seen¹. The parabolic trajectory that optical Airy beams follow in free space during propagation is analogous to those of projectiles moving under the action of a uniform gravitational fields and this behavior is described in detail in Ref.4.

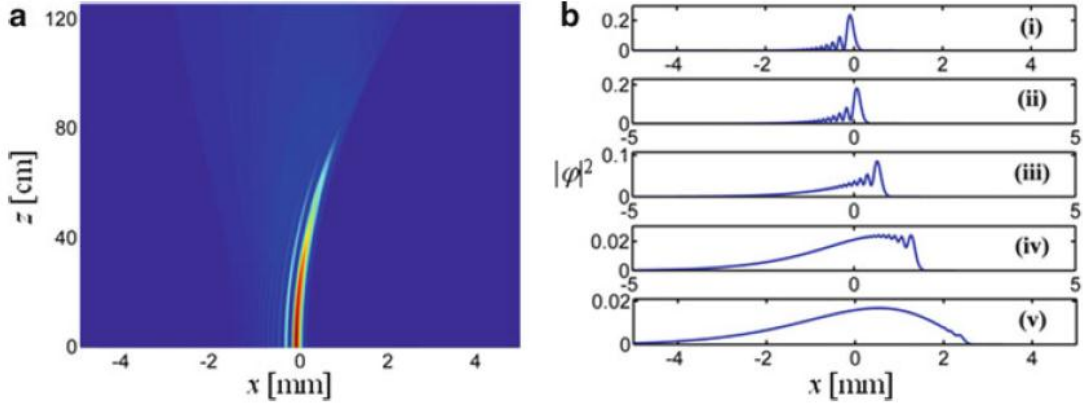


Figure 1.2| (a) Propagation dynamics of a finite-energy Airy beam as a function of distance, (b) cross sections of the normalized beam intensity at different propagation distances over z .

1.3 Experimental observation of 1D and 2D Finite Airy beams

The experimental observation of 1D and 2D Airy beams was performed in Ref. 2. The Fourier transform $\Phi_0(k)$ of the finite norm wave packet described by Eq.1.4 is proportional to $\Phi_0(k) \propto \exp(-\alpha k^2) \exp(i \frac{k^3}{3})$ [1]. From this equation, it is easily observed that the angular Fourier spectrum of the finite Airy beam is Gaussian and involves a cubic phase (k^3) resulting from the Fourier transform of the Airy function itself. This result has great significance for the experimental generation of such beams. These waves can be generated through the Fourier transform (FT) of a broad Gaussian beam in which will be imprinted the specific cubic phase. So, for the experimental study of a finite –energy Airy wave packet the fact that the FT of the function $\text{Ai}(s) \exp(\alpha s)$ is a Gaussian beam modulated with a cubic phase, was considered. The cubic phase modulation of a Gaussian beam was succeeded using a computer-controlled liquid crystal spatial light modulator (SLM) which can impose a cubic phase to the reflected beam, necessary for the Airy beam generation. Examples of phase masks used for the phase modulation of a Gaussian beam by the SLM are shown in Figure 1.3a,b while a typical set-up for Airy beam generation is illustrated in Figure 1.3c. A continuous-wave laser emits a linearly polarized Gaussian beam that is then reflected from the front facet of a SLM. For the Airy beam generation

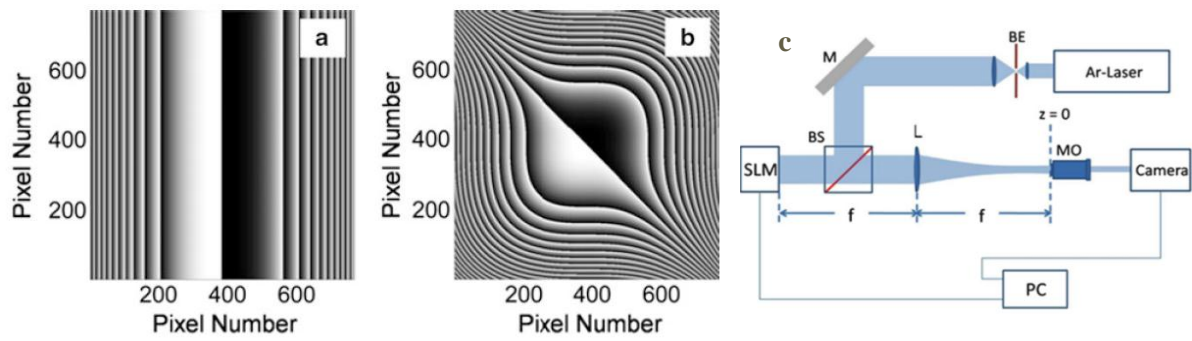


Figure 1.3] Phase masks used to generate (a) 1D and (b) 2D-Airy beams. The cubic phase is «wrapped» between $[0, 2\pi]$. In the gray-scale pattern, black corresponds to 0 and white to 2π radians (c) Experimental setup for generation of truncated Airy beams. SLM spatial light modulator, BE beam expander, MO microscope objective. [2]

an appropriate Fourier transform lens (cylindrical for 1D and spherical for 2D Airy) is placed at a distance f in front of the SLM phase array. After the SLM, the FT of the phase modulated Gaussian beam is then obtained at a distance $d=f$ behind the lens. The Airy beam produced is imaged on a CCD camera through a microscope objective. Observed intensity distributions of 1D and 2D Airy beams are shown in Figure 1.4. From figure 1.4A we observe the the finite airy intensity profile remains almost diffraction – free while its main lobe tends to quadratically accelerate. The diffraction dynamics of the 2D Airy beams are interesting too [Figure 1.4B].

So, the experimental illustration of Airy beams confirmed the exotic characteristics of these beams, like that they are diffraction free during propagation and freely accelerating.

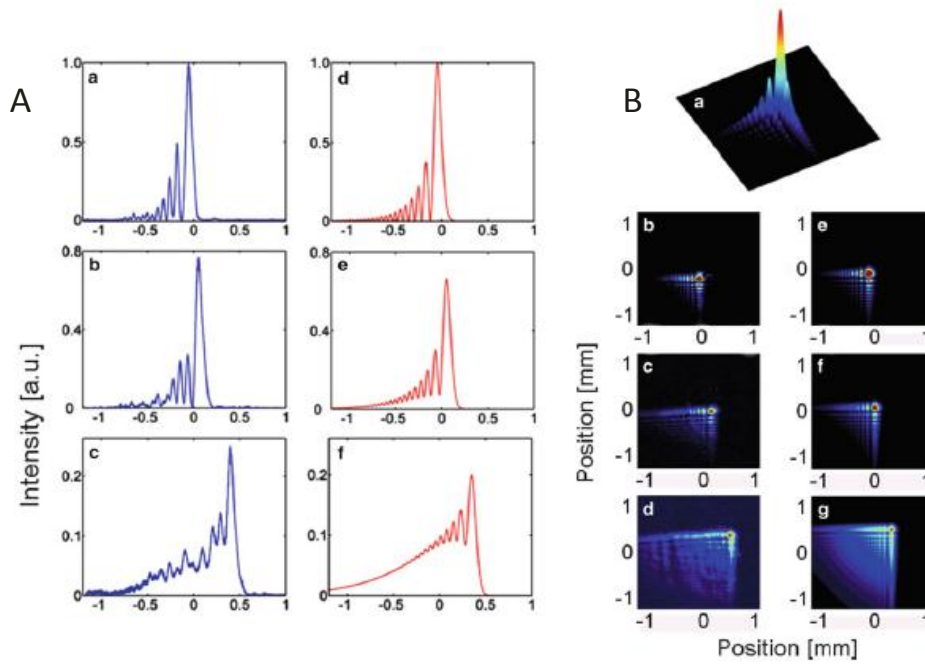


Figure 1.4|A. Observed intensity cross sections of a planar Airy beam at (a) $z=0$ cm, (b) 10 cm, and (c) 20 cm. Corresponding theoretical plots for these same distances (d), (e) and (f). **B.** (a) A schematic of a 2D Airy packet. Observed intensity distribution of a 2D Airy beam at (b) $z=0$ cm, (c) 10 cm, and (d) 20 cm. Corresponding theoretical results at these same distances (e), (f), and (g) [2]

1.4 Radially Symmetric Autofocusing Beams

It is the past few years that a new type of 2D and 3D Airy waves that tend to autofocus in an abrupt fashion was introduced [8]. Radially symmetric Airy beams or ring-Airy beams abruptly autofocus, delivering high intensity contrast at the focal position. The maximum intensity of such a radial wave remains almost constant during propagation while it suddenly increases by orders of magnitude right before its focal point. The ring-Airy distribution is described by:

$$u_0(r,0) = Ai\left(\frac{r_0-r}{w}\right) \exp\left[\alpha \cdot \left(\frac{r_0-r}{w}\right)\right], \quad (1.5)$$

where $Ai(\cdot)$ denotes the Airy function [1, 8], r is the radius, r_0 is the radius of the primary ring, w is a scaling factor and α an exponential decay factor. The radius of the highest intensity Airy ring is given by $R_0 \cong (r_0 + w)$ while its full width at half maximum (FWHM) is $\cong 2.28w$, which corresponds to the average width of the primary ring (ref. 4). The distance between the plane of generation of the ring Airy distribution and its focus position (ref. 4) can be defined as the effective focal length $f_{Ai} = (4\pi w^3 / \lambda) R_0^{1/2}$ (1.6). From Eq. 1.6 we can see

that the effective focus position of a ring Airy beam can be controlled by the w and r_0 parameters. The radius $R(z)$ of the primary Airy is described by $R(z) \cong (r_0 - w) - 3.15 \cdot 10^{-3} \left(\frac{\lambda^2}{w^3}\right) z^2$ (1.7). By using Eqs. 1.6 & 1.7 we can describe the radius of the primary Airy ring as a function of the initial radius $R(0)$ and the effective focal length f_{Ai} :

$$R(z) \cong R(0) \left(1 - \frac{z^2}{f_{Ai}^2}\right) \quad (1.8) .$$

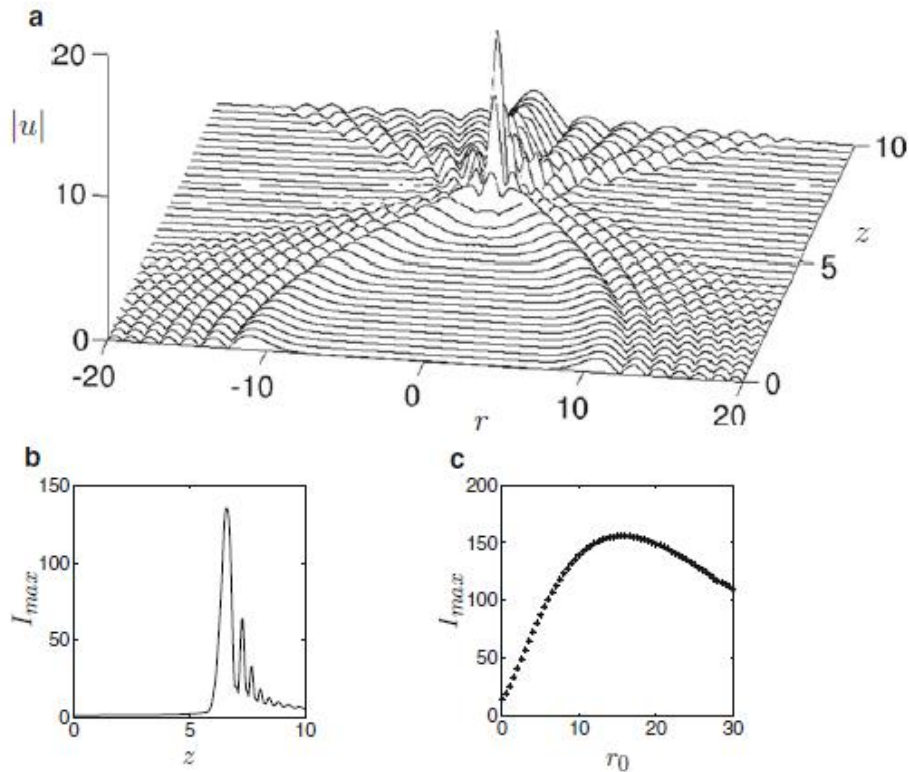


Figure 1.5 Dynamics of radially symmetric Airy beams. (a) Detailed plot of the central part of the propagation dynamics; (b) Maximum intensity as a function of z ; (c) Maximum intensity that the Airy beam reaches during propagation for different values of the initial radius r_0 . [8]

The propagation dynamics of a ring-Airy beam is depicted in Figure 1.5 [8]. We can describe the propagation dynamics of these beams as following: in the early stages of propagation, r_0 is large enough and the disk $r < r_0$ is essentially dark. As z increases, the radius of the Airy beam decreases, the power concentrates in a smaller area, and the maximum amplitude increases. In fact, the numerical simulations show that these two effects almost balance each other, leading to relatively small maximum amplitude changes, up to the point where the beam reaches the center (Fig. 1.5a, b). At the focal point, the power of the ring-Airy is concentrated in a small area around $r = 0$ and the maximum intensity at the center rapidly increases.

These radially symmetric autofocusing Airy beams have been recently experimentally generated⁹. The cylindrically symmetric Airy beams (ring-Airy beams) were able to abruptly autofocus, along their propagation, delivering high intensity contrast at the focus position. It is also quite interesting the fact that such beams present long working distances, tight focusing and small focal volumes (ref. 9) while nonlinear propagation effects can be very exciting (ref. 10). These notable properties can be seen in Figures 1.6 A & B. For the experimental realization of the ring-Airy beams an optical set-up as the one shown in Figure 1.7 was used. In this case, the FT of the radially symmetric Airy distribution was firstly encoded onto a phase filter, which is applied onto a phase-only reflecting spatial light modulator (SLM) screen (Hamamatsu LCOS-X10468-2), as shown in Fig. 1.7. The phase modulation capability of this device is up to $\sim 2\pi$ therefore phase wrapping is used to implement higher phase modulation. The phase modulated reflected wavefront is then Fourier transformed by a lens (f). An opaque mask was used to block the undesired zero-order peak. Finally, the intensity distribution along the propagation is recorded using a linear CCD camera (12 bits, 1224×968 pixels).

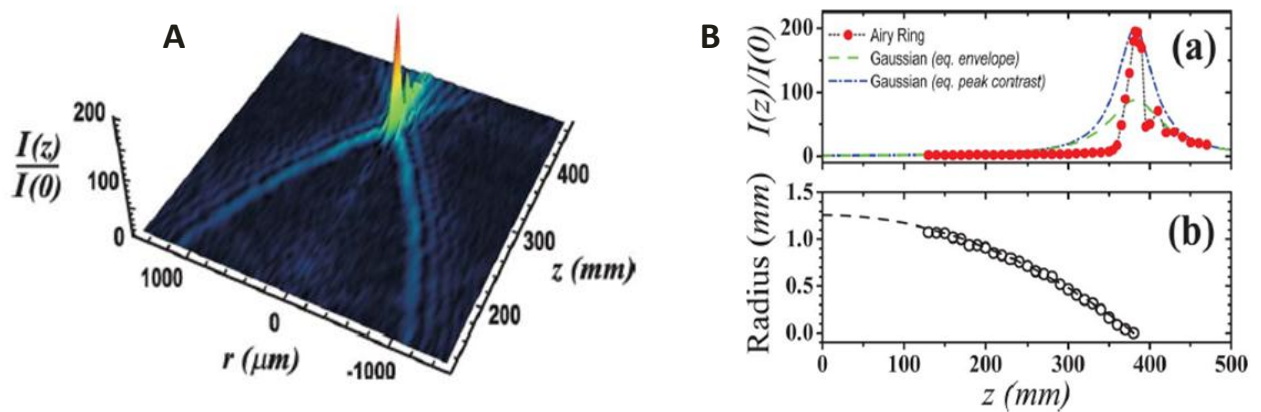


Figure 1.6 **A** Radially averaged intensity as a function of the propagation distance. **B** (a) Intensity contrast as a function of the propagation distance: solid circles, experimental values; dashed curve and dashed-dotted curve, intensity contrast of equivalent Gaussian beams. (b) Radius of the ring Airy as a function of the propagation distance: open circles, experimental points; dashed curve, quadratic fit. [9]

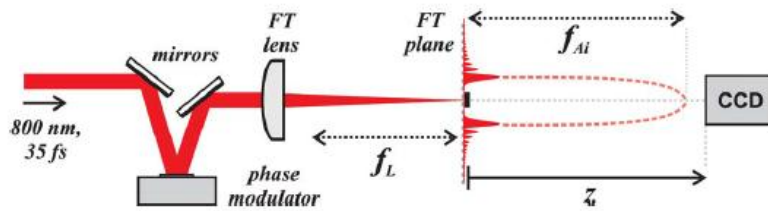


Figure 1.7 | Typical experimental setup. FT, Fourier transform; f_L , FT lens focal length; f_{Ai} , effective focal length of the Airy ring.

A representation of the clear advantage of the autofocusing waves in laser processing of thick samples is shown in Figure 1.8a. It is obvious that, by using these beams, a long working distance can be combined with a short focal volume, thanks to the abrupt increase of the intensity of the Airy ring at the focus. Thus, these beams are great candidates for many applications like nanosurgery. As a simple example of the power of this approach, we show in Fig. 1.8b an ablation spot produced in the back side of a thick (10mm) fused silica window using our intense Airy ring beam. It is also quite exciting that this beam will not be destructive before the focus while it abruptly deliver high intensity contrast at the focus position.

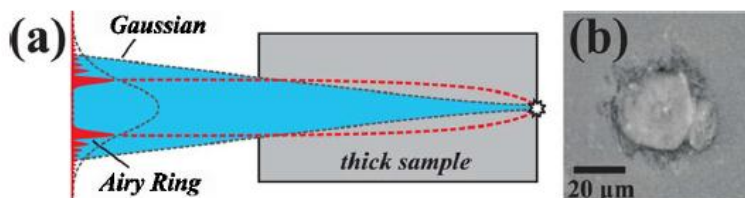


Figure 1.8 | (a) Processing of a thick sample. Comparison of a ring-Airy with a Gaussian beam of similar spot size (b) ablation crater in the back side of a 1cm thick fused silica sample after illumination by an intense ring-Airy beam.

References

1. Siviloglou, G. A. & Christodoulidis, D.N. Accelerating finite energy Airy beams. *Opt. Lett.* **32**, 979-981 (2007)
2. Siviloglou, G. A., Broky, J., Dogariu A., & Christodoulidis, D.N Observation of accelerating airy beams. *Phys. Rev. Lett.* **99**,213901 (2007)
3. M.V. Berry, N.L. Balazs, *Am. J. Phys.* **47**, 264 (1979)
4. Siviloglou, G. A., Broky, J., Dogariu A., & Christodoulidis, D.N. Ballistic dynamics of Airy beams. *Opt. Lett.* **33**, 207-209 (2008)
5. J. Baumgartl, M. Mazilu, K. Dholakia, *Nat. Photonics* **2**, 675 (2008)
6. P. Zhang, J. Prakash, Z. Zhang, M.S. Mills, N.K. Efremidis, D.N. Christodoulides, Z. Chen, *Opt. Lett.* **36**, 2883 (2011)
7. Z. Zheng, B. Zhang, H. Chen, J. Ding, H. Wang, *Appl. Opt.* **50**, 43 (2011)
8. N.K. Efremidis, D.N. Christodoulides, *Opt. Lett.* **35**, 4045 (2010)
9. D.G. Papazoglou, N.K. Efremidis, D.N. Christodoulides, S. Tzortzakis, *Opt. Lett.* **36**, 1842 (2011)
10. P. Panagiotopoulos, D. G. Papazoglou, A. Couairon, and S. Tzortzakis, Sharply autofocused ring-Airy beams transforming into non-linear intense light bullets, *Nat. Commun.* **4**, 2622 (2013).

2.1 Introduction

In chapter one, we noticed that Airy beams can be generated through the Fourier transform (FT) of a Gaussian beam in which a specific cubic phase should be imprinted. The angular Fourier spectrum (Eq.1.5) of the finite Airy beam is Gaussian and involves a cubic phase (k^3) resulting from the Fourier transform of the Airy function itself. So, the phase of the Gaussian beam should be first properly modulated in order the Airy distribution to be generated. In this chapter we will discuss the method to modulate the phase of a Gaussian beam in order beam shaping to be achieved.

2.2 General Shaping problem

Laser beam Shaping is the process of redistributing the phase and /or the amplitude of a beam. The phase of the shaped beams is a major factor in determining the propagation dynamics and properties of the shaped beam profile. For example, a large beam with a uniform phase front will maintain its shape over a considerable propagation distance. Also, the beam shaping technology can be applied to both coherent and incoherent beams. The general beam shaping problem is illustrated in Figure 2.1. An incident beam is inserted in a general optical system

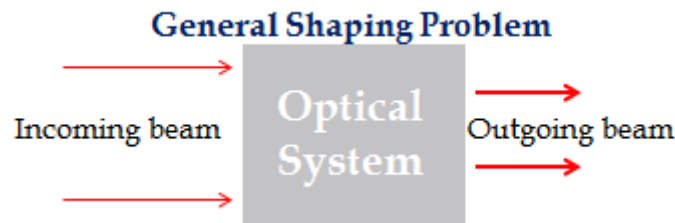


Figure 1.3| General beam Shaping problem

which is consisted of one or more optical elements. The input beam is transformed due to the optical system operation, and the desired output beam is produced.

The keyword to understand, though, how we shape the light, is the Phase Modulation. Let's start with the Harmonic plane wave's equation:

$$U(\mathbf{r}, t) = u_0 e^{i(\mathbf{k} \cdot \mathbf{r} - \omega t)}, \quad \mathbf{k} \equiv n \frac{2\pi}{\lambda_0} \hat{\mathbf{k}} \quad (2.1),$$

where \mathbf{k} is the wave vector normal to the wavefront, n is the refractive index, u_0 is the wave's amplitude. The term $(\mathbf{k} \cdot \mathbf{r} - \omega t)$ describes the phase of the wave. If now we assume that the wave propagates along z axis:

$$\left. \begin{aligned} \hat{k} &\equiv \hat{z}, \\ k &\equiv n \frac{2\pi}{\lambda_0} \hat{k} \end{aligned} \right\} \quad k \equiv n \frac{2\pi}{\lambda_0} \hat{z} \quad \rightarrow \quad \mathbf{k} \cdot \mathbf{r} = \frac{2\pi}{\lambda_0} n \cdot z \quad (2.2)$$

Relation 2.2 corresponds to the optical path i.e. the path that light follows when travelling through an optical system. So the harmonic wave equation becomes:

$$U(\mathbf{r}, t) = u_0 e^{i(\frac{2\pi}{\lambda_0} n \cdot z - \omega t)} \quad (2.3)$$

From equations 2.2 & 2.3, we observe that the modulated phase of a plane wave can be derived by measuring the optical path length that a beam follows when interacts with an optical system. So, phase is equivalent to the optical path: Phase \equiv Optical Path. The latter result facilitates the problem of phase determination for beam shaping. We can shape the wavefront of a beam by spatially controlling the optical path length (OPL) of each point in the wavefront. The OPL is defined by the product of the refractive index n of a specific medium, with the physical length d of the medium, $OPL = n \cdot d$ (2.4). In Figure 2.2 a general wave

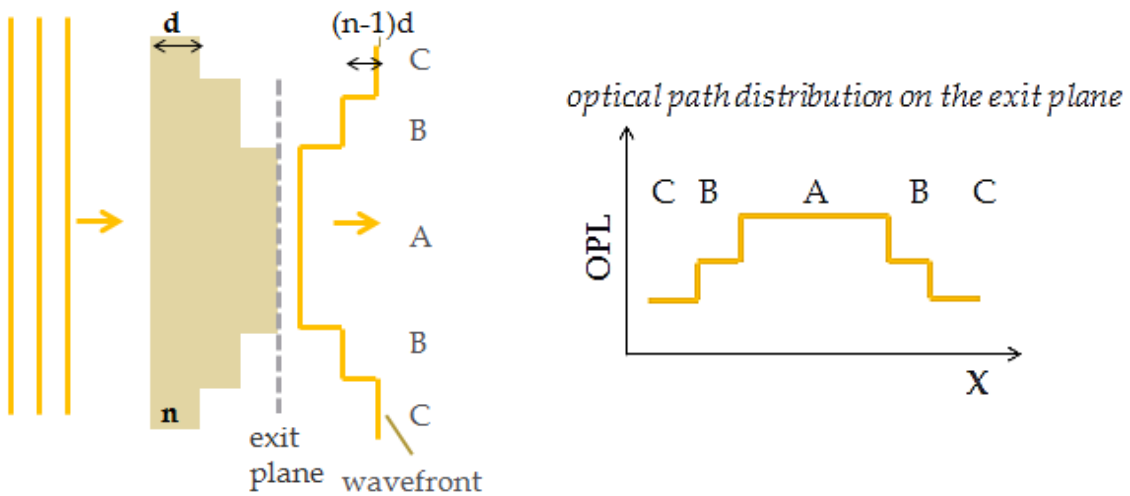


Figure 2.2| Wavefront shaping by an optical element of refractive index n . [1]

front shaping problem of a beam due to an optical element is represented. Plane waves incidence upon an optical element with refractive index (R.I.) n , and the modulation of the outgoing wave front due to the different optical path lengths that the light follows point by point, can be seen behind the exit plane. At this point is interesting to calculate the optical path difference which corresponds to the phase shift that occurs when the wave passed through the material with R.I. n (for example glass) appearing to travel a greater distance than an identical wave in air. So, we have:

$$\begin{array}{l}
 (OPL)_A = 3n \cdot d \\
 (OPL)_B = 2n \cdot d + d \\
 (OPL)_C = 2n \cdot d + 2d
 \end{array}
 \left. \vphantom{\begin{array}{l} (OPL)_A \\ (OPL)_B \\ (OPL)_C \end{array}} \right\} \rightarrow \Delta L = (OPL)_A - (OPL)_B \\
 \hspace{15em} = (OPL)_B - (OPL)_C = (n - 1)d \quad [1]$$

where, ΔL is the optical path difference. As a result, controlling the optical path difference we can determine the phase difference and the phase modulation would appear to the beam. The most usual example of wavefront reshaping is the action of simple converging or diverging lenses. In that case a plane wavefront is converted to a spherical one (Figure 2.3). Each plane wavefront travels a different optical path distance, and the front reshapes.

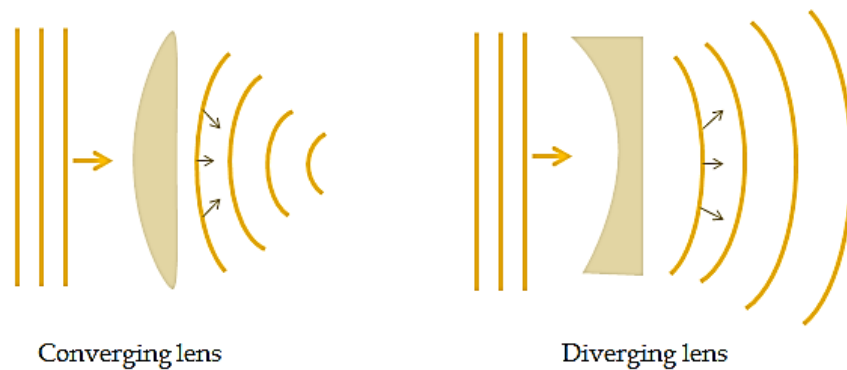


Figure 2.3| Wavefront shaping by converging/diverging lenses: plane wave is reshaped to a spherical.

2.3 Fourier Transform approach

As discussed before, we not only need to modulate the phase of a Gaussian beam but also to use Fourier transform analysis for the generation of the Airy distribution. Fourier optics is the study of classical optics using Fourier transforms. Fourier optics features the meaning of the propagation of light wave on the basis of harmonics analysis and linear systems. Harmonic analysis is the Fourier transform whose methods can be used to analyse signals and systems in several areas.[2] Linear systems are used for formulating diffraction as well as imaging. If there is an input, the system forms an output. Therefore, it can be understood that the system is an input-output mapping [3] In Fourier optics, the wave is regarded as a superposition of plane waves. The plane wave spectrum concept is the basic foundation of Fourier Optics. The plane wave spectrum is a continuous spectrum of uniform plane waves, and there is one plane

wave component in the spectrum for every far field distribution. The assumption of plane waves was also used to describe the general beam shaping problem to the paragraph 2.2. This paragraph describes a diffraction- based method for converting a Gaussian beam into a different beam profile. The design is based on Fourier Transform relation between the input and output beam functions.

In order to understand the operation of Fourier optics in the optical systems, we will describe the Fourier Transforming property of a lens. In Figure 2.5, we observe a plane wave incident to a phase element (i.e. a diffractive optic). After the phase object, the beam seems to be modulated. If the phase object is placed one focal length in front of a lens, then its **Fourier Transform** will be formed one focal length behind the lens. Such a lens is called Fourier transform lens. At the Fourier transform (FT) plane of the FT lens, the desired beam distribution is appeared.

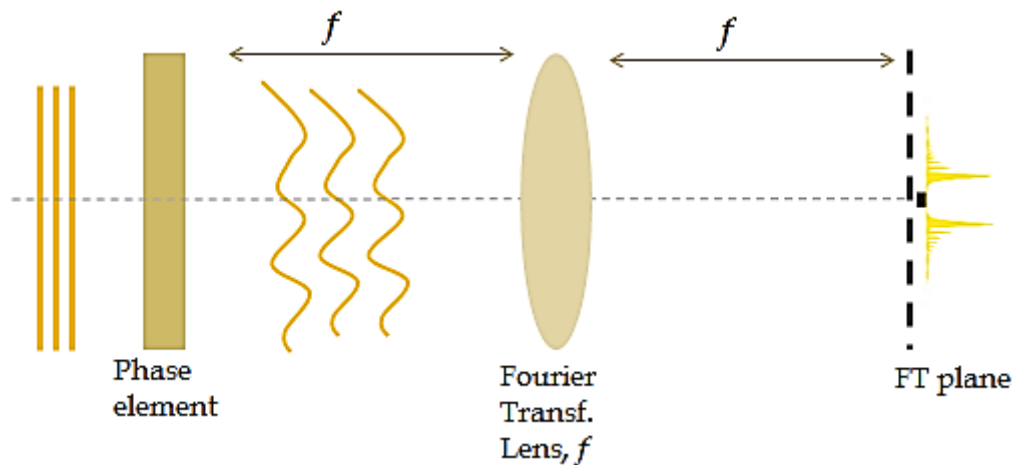


Figure 2.4 Fourier Transforming property of a lens

This is the general idea of the Fourier Transforming approach in an optical system for beam reshaping. We would like to choose the beam shaping element so that the output at the FT plane has the desired intensity distribution. This configuration has several advantages. The phase element can be changed to control both the scale and shape of the output irradiance, while the FT lens can be changed to modify the working distance, with a corresponding change in scale of the output.

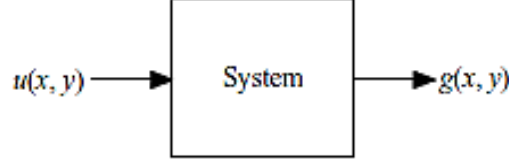


Figure 2.5 | $u(x,y)$ is the input signal, and $g(x,y)$ is the output signal in an optical system. [3]

Before we continue, it is interesting to see the 2-D convolution theorem resulting from an input-output optical system as shown in Figure 2.5. In a linear system, a given input transforms into a unique output. The 2D system in Figure 2.4, shows an input field $u(x,y)$ and an output signal $g(x,y)$. We can mathematically represent this system as:

$$g(x,y) = O[u(x,y)] \quad (2.5)$$

The system is called linear if any linear combination of two inputs $u_1(x,y)$ and $u_2(x,y)$ generates the same combination of their respective outputs $g_1(x,y)$ and $g_2(x,y)$. This is called *superposition principle*. Let us now suppose that the input at (x_1, y_1) is the delta function $\delta(x_1, y_1)$. Then the output at location (x, y) is defined as

$$h(x, y; x_1, y_1) = O[\delta(x - x_1, y - y_1)] \quad (2.6)$$

We can rewrite the input as:

$$u(x, y) = \int_{-\infty}^{+\infty} \int_{-\infty}^{+\infty} u(x_1, y_1) \delta(x - x_1, y - y_1) dx_1 dy_1 \quad (2.7)$$

From formulas (2.5), (2.6) & (2.7), the output can be rewritten as

$$g(x, y) = \int_{-\infty}^{+\infty} \int_{-\infty}^{+\infty} u(x_1, y_1) \delta(x - x_1, y - y_1) dx_1 dy_1 = \int_{-\infty}^{+\infty} \int_{-\infty}^{+\infty} u(x_1, y_1) h(x, y; x_1, y_1) dx_1 dy_1 \quad (2.8)$$

The integral (2.8) is called the superposition integral

If the input is shifted as $\delta(-x_1, -y_1)$, the output of a shift-invariant system must be $h(x-x_1, y-y_1)$.

Then, the superposition integral becomes

$$g(x, y) = \int_{-\infty}^{+\infty} \int_{-\infty}^{+\infty} u(x_1, y_1) h(x - x_1, y - y_1) dx_1 dy_1 \quad (2.9)$$

Or by a change of variables:

$$g(x, y) = \int_{-\infty}^{+\infty} \int_{-\infty}^{+\infty} h(x_1, y_1) f(x - x_1, y - y_1) dx_1 dy_1 \quad (2.10)$$

This is the 2-D convolution of $h(x,y)$ with $u(x,y)$ to yield $g(x,y)$. It is

often written symbolically as

$$g(x, y) = h(x, y) * u(x, y) \quad (2.11)$$

The significance of this result is that a linear optical system is governed by convolution. Hence, the convolution theorem can be used to express the input-output relationship as

$$G(f_x, f_y) = H(f_x, f_y)U(f_x, f_y) \quad (2.12)$$

where $G(f_x, f_y)$, $H(f_x, f_y)$ & $U(f_x, f_y)$ are the Fourier transforms of $g(x, y)$, $h(x, y)$ & $u(x, y)$, respectively. The $H(f_x, f_y)$ function is called the transfer function of the optical system and is given by

$$H(f_x, f_y) = \int_{-\infty}^{+\infty} \int h(x, y)e^{-j2\pi(f_x x + f_y y)} dx dy \quad (2.13),$$

corresponding to the 2D Fourier transform of $h(x, y)$ [3]

Next, we will discuss the use of lenses to form the Fourier transform or the image of an incoming coherent wave. When light passes through a lens, it undergoes a phase transform (Figure 2.4(a)). A lens consists of an optically dense material in which the phase velocity is less than the velocity in air. The thickness of the lens is modulated so that a desired phase modulation is achieved at the aperture of the lens. A thin lens has three important parameters: n , the material index of refraction by which factor the phase velocity is reduced, R_1 and R_2 , which are the radii of the two circular faces of the lens. The three parameters discussed about can be combined in a single parameter called f , the focal length, by:

$$\frac{1}{f} = (n - 1)\left(\frac{1}{R_1} - \frac{1}{R_2}\right) \quad (2.14)$$

The phase transformation of a lens can be written as

$$t(x, y) = e^{-jkt_0} e^{-j\frac{k}{2f}(x^2 + y^2)} \quad (2.15),$$

where t_0 is the maximum thickness of the lens and e^{-jkt_0} gives a constant phase change.[3]

We can define a pupil function $P(x, y)$ for the finite extent of the lens aperture :

$$P(x, y) = \begin{cases} 1, & \text{inside the lens aperture} \\ 0, & \text{otherwise} \end{cases} \quad (2.16)$$

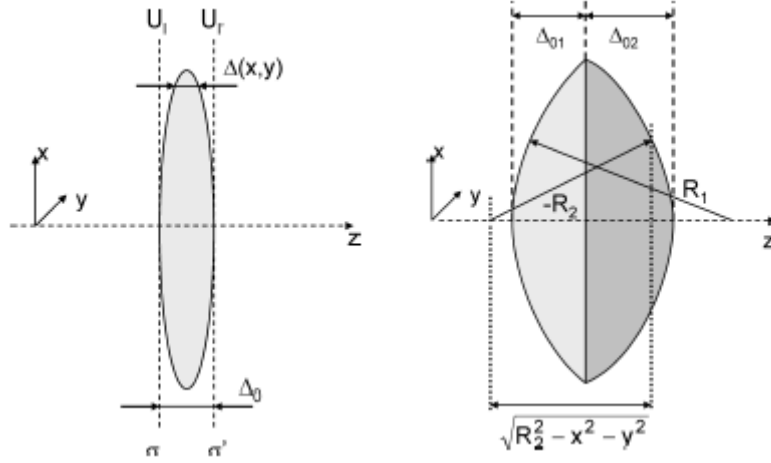


Figure 2.6 | A thin lens (left); Parameters of a thin lens (right) [4]

The thickness $\Delta(x,y)$ at a location (x,y) can be shown to be

$$\Delta(x,y) = t_0 - R_1 \left(1 - \sqrt{1 - \frac{x^2+y^2}{R_1^2}}\right) + R_2 \left(1 - \sqrt{1 - \frac{x^2+y^2}{R_2^2}}\right) \quad (2.17)$$

We can simplify the expression (2.17) using the paraxial approximation stated by

$$\sqrt{1 - \frac{x^2+y^2}{R_i^2}} \cong 1 - \frac{x^2+y^2}{2R_i^2} \quad (2.18), R_i \text{ denotes } R_1 \text{ or } R_2$$

The phase transformation is expressed as

$$\theta(x,y) = kn\Delta(x,y) + k(t_0 - \Delta(x,y)) = kt_0 + k(n-1)\Delta(x,y) \quad (2.18)$$

Using Eq. (2.14) & (2.17), Eq. (2.18) becomes

$$\theta(x,y) = kt_0 - \frac{k}{2f}(x^2 + y^2) \quad (2.19)$$

Then Eq. 2.19 leads to Eq. 2.15.

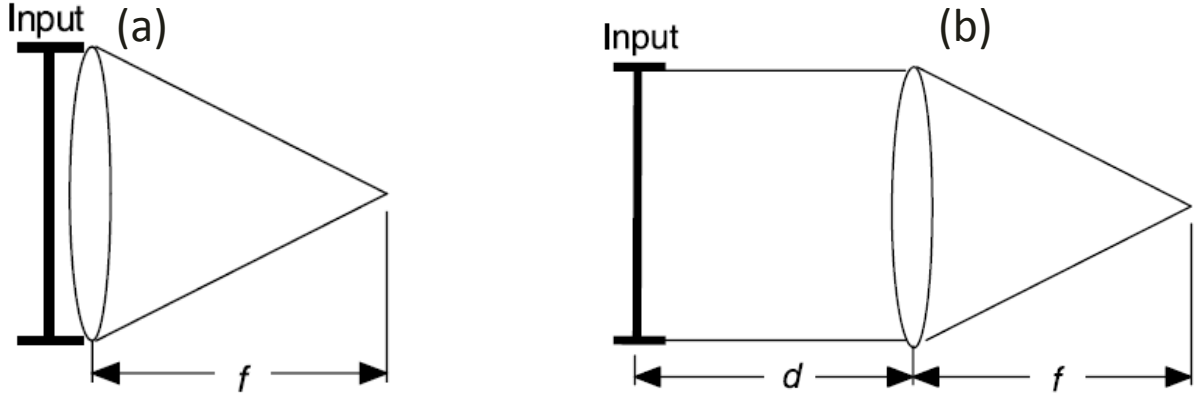


Figure 2.7 | The geometry for input placed: (a) against the lens; (b) to the left of the lens [3]

Suppose now that a phase element is positioned against a lens as shown in Figure 2.7(a). The wave field incident the lens is $U(x, y, 0)$. According to expressions (2.15), (2.16) and the convolution theorem discussed before, the wave field behind the lens is given by

$$U'(x, y, 0) = U(x, y, 0)P(x, y) e^{j\frac{k}{2f}(x^2 + y^2)} \quad (2.20)$$

According to the Fresnel diffraction integral stated by:

$$U(x_0, y_0, z) = \frac{e^{jkz}}{j\lambda z} e^{j\frac{k}{2\pi}(x_0^2 + y_0^2)} \iint_{-\infty}^{+\infty} U'(x, y, 0) e^{j\frac{2\pi}{\lambda z}(x_0x + y_0y)} dx dy \quad (2.21)$$

,the wave field at $z=f$ with focal plane coordinates to be (x_f, y_f, f) is given by

$$U(x_f, y_f, z) = e^{j\frac{k}{2f}(x_f^2 + y_f^2)} \iint_{-\infty}^{+\infty} U'(x, y, 0)P(x, y, 0) e^{j2\pi(f_x x + f_y y)} dx dy \quad (2.22)$$

Consider the geometry in Figure 2.7(b) where a phase element is deposited to the left of the lens. The wave field at the plane $Z=-d$, $d>0$ is given by $U(x_1, y_1, -d)$. Its angular spectrum $\mathcal{F}(fx, fy, -d)$ and the angular spectrum $\mathcal{F}(fx, fy, 0)$ of $U(x, y, 0)$ are related by

$$\mathcal{F}(fx, fy, 0) = \mathcal{F}(fx, fy, -d) e^{-j\pi\lambda d(f_x^2 + f_y^2)} \quad (2.23)$$

We can write 2.22 as
$$U(x_f, y_f, z) = \mathcal{F}(fx, fy, 0) e^{j\frac{k}{2f}(1 - \frac{d}{f})(x_f^2 + y_f^2)} \quad (2.25)$$

When $d=f$, the phase factor becomes one and the Eq.(2.25) is written as

$$U(x_f, y_f, z) = \mathcal{F}(fx, fy, -f) \quad (2.26)$$

Expression (2.26) represents that the wave field at the focal plane of the lens is the 2-D Fourier transform of the wave field at $z = -f$. This notable result confirms the Fourier Transform analysis presented in Figure 2.4.

2.4 Fourier Transform in 4F optical correlator

A quite interesting device which implements the Fourier transform approach and the theory of convolution is the $4f$ correlator. In this case two lenses and a phase mask are used while the device is $4f$ long. A typical $4f$ optical correlator diagram is shown in Figure 2.8.

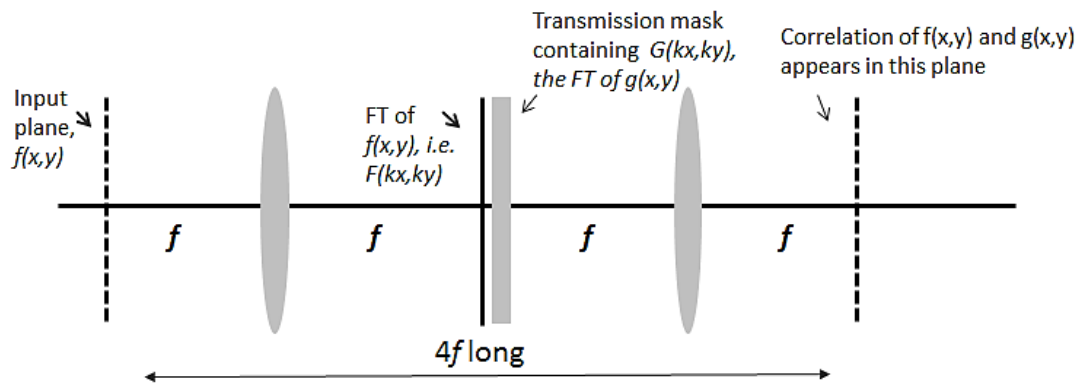


Figure 2.8 | The $4f$ optical correlator

The $4f$ correlator is based on the convolution theorem from Fourier transform theory, which states that convolution in the spatial (x, y) domain is equivalent to direct multiplication in the spatial frequency (k_x, k_y) domain. A plane wave is assumed incident from the left and a transparency containing one 2D function, $f(x, y)$, is placed in the input plane of the correlator, located one focal length in front of the first lens. The transparency spatially modulates the incident plane wave in magnitude and phase and produces a spectrum of plane waves corresponding to the FT of the transmittance function ($f(x, y)$). That spectrum is then formed as an "image" one focal length behind the first lens, as shown. A transmission mask containing the FT of the second function, $g(x, y)$, is placed in this same plane, one focal length behind the first lens, causing the transmission through the mask to be equal to the product, $F(k_x, k_y) \times G(k_x, k_y)$. The FT of this product (i.e., the convolution of $f(x, y)$ and $g(x, y)$), is formed in the back focal plane of the second lens.

The FT plane mask function, $G(k_x, k_y)$ is the system transfer function of the correlator, which is in general denoted as $H(k_x, k_y)$. In the $4f$ correlator, the system transfer function $H(k_x, k_y)$ is directly multiplied against the spectrum $F(k_x, k_y)$ of the input function, to produce the spectrum of the output function. (Eq. 2.11, 2.12)

2.5 Spatial Light Modulator

In Chapter One we saw that a Gaussian beam was phase modulated by a Spatial Light Modulator or SLM (Figure 1.8). A SLM can be placed in the back focal plane of a Fourier transforming lens, where it modifies the transmitted or reflected fields in accord with a desired complex spatial filter. This device would appear at the position of the phase element in Figure 2.4. A spatial light modulator is an object that imposes some form of spatially varying modulation on a beam of light and is usually computer controlled. SLMs can be programmed to produce light beams with various optical wavefronts by taking the place of conventional optical elements. For instance, they can be used to create optical vortices and higher order Bessel beams, which both have an azimuthal phase variation.

There is a broad categorization of SLMs into two classes that can be made at the start: (1) electrically addressed SLMs and (2) optically addressed SLMs. In the first case, electrical signals representing the information to be input to the system directly drive a device in such a way as to control its spatial distribution of absorption or phase shift. In the latter case, the information may be input to the SLM in the form of an optical image at the start rather than in electrical form.

In the experimental part of this master thesis, a Liquid Crystal on Silicon-Spatial Light Modulator (LCOS-SLM) is going to be employed in order a Gaussian beam to be modulated by a cubic phase and the Fourier transformation of the modulated beam, to be redistributed in a radially symmetric Airy beam. So, here we will limit ourselves to presenting the barest outlines of the principles of operation of liquid crystal SLMs. The LCOS-SLM (Liquid Crystal on Silicon-Spatial Light Modulator) is a reflection type spatial light modulator that freely modulates the light phase as needed.

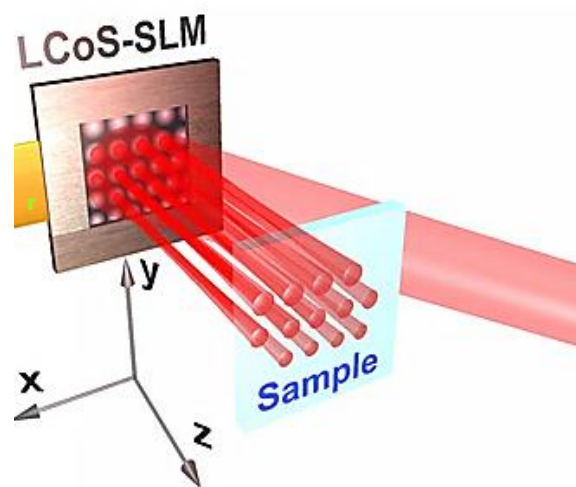


Figure 2.9| Liquid crystal Spatial Light modulator.[5]

A light beam such as a laser beam entering the LCOS-SLM is phase-modulated and then reflected to freely control the wavefront of (reflected) light as needed. This ability to accurately control the light wavefront makes the LCOS-SLM ideal for applications such as optical beam pattern forming [7]. The LCOS display consists of a parallel-aligned nematic liquid crystal layer used to modulate light (Figure 2.10). Phase modulation is changed according to the alignment of the liquid crystals (LC). The LC alignment is controlled, pixel by pixel, using a CMOS backplane and a DVI signal via a PC. Voltages applied to pixelated electrodes cause the polarization change of the LCs. Liquid crystal materials are interesting from a physical point-of-view because they share the properties of both solids and liquids.

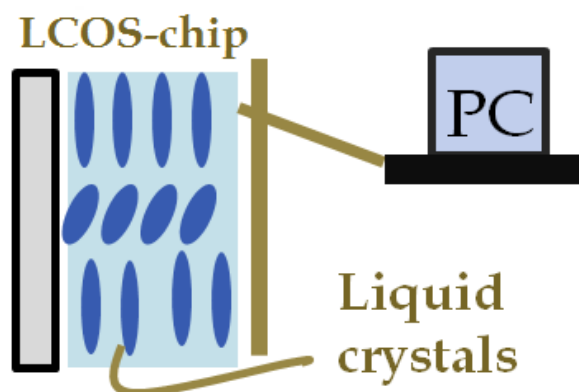


Figure 2.10 Side view of a LCOS modulator with nematic liquid crystals.

This rod- molecules composing such materials can be visualized as ellipsoids, with a single long axis. The molecules can rotate or slide with respect to one another under the application of mechanical or electrical forces, thus exhibiting some of the properties of a liquid. Another important quality is that, similar to many crystalline materials, liquid crystals are birefringent, meaning they have different indices of refraction associated with different crystallographic directions. This is because the binding forces that form the crystal are anisotropic, i.e. the atoms have stronger forces holding them together in certain crystalline directions. The long axis of the molecules is known as the slow axis, where rays experience a higher index of refraction and are therefore bent more. If light enters a liquid crystal molecule with its polarization axis parallel to the slow axis of the molecule this extraordinary ray will be slowed down; the rays will travel faster when the polarization axis is perpendicular to the slow axis. Therefore, phase modulation occurs as the liquid crystal molecule is tilted from

having the polarization axis of incoming light parallel to the slow axis to perpendicular to the slow axis (Figure 2.11).

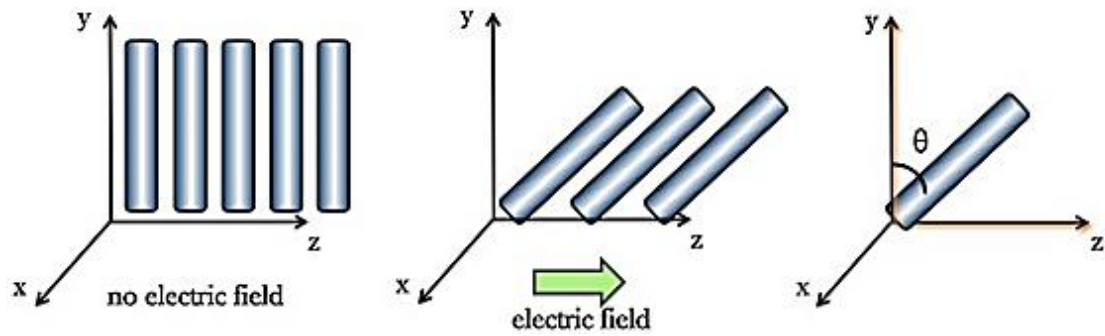


Figure 2.11| Parallel-aligned nematic liquid crystals, without or with electric field.[7]

Spatial light modulators are used to spatially modify an optical wavefront into almost any desired field distribution, while it can replace the dynamic operation of every optical element (i.e. lenses, axicon, grating e.t.c.) In Figure 2.12 three basic examples of shaped light beams are represented, confirming the dynamics of this device.

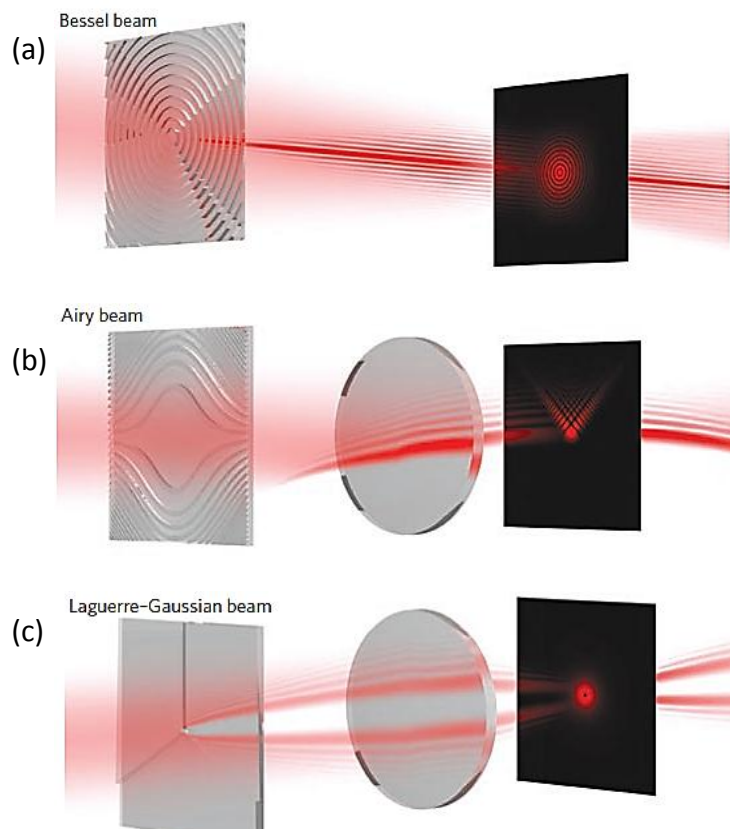


Figure 2.11| Basic examples of shaped light beams using as Spatial Light Modulator [6]

In Figure 2.11(a) a non-diffracting Bessel beam generated by a diffraction Axicon applied onto a spatial light modulator display is performed, while in figure 2.11(b) an Airy beam is generated by a diffractive cubic phase mask in the back focal plane of a FT lens. Finally, an optical vortex beam is generated by a helical phase mask produced by the SLM and then focused by a lens.

References

1. Based on Phase Control Tutorial by Prof. Dimitri Papazoglou
2. Saleh, B. E. A., & Teich, M. C. (1991). *Fundamentals of photonics*. New Jersey: John Wiley & Sons. Inc.
3. Ersoy, O. K. (2007). *Diffraction, Fourier optics And imaging*. New Jersey: John Wiley & Sons, Inc.
4. J. W. Goodman.(1968). *INTRODUCTION TO FOURIER OPTICS*. McGraw-Hill, New York
5. Ruediger Grunwald and Martin Bock,SPIE Newsroom.DOI: 10.1117/2.1201003.002866
6. K.Dholakia and T.Cizmar , Nature Photonics doi: 10.1038/nphoton.2011.80

Links

7. <http://www.hamamatsu.com/jp/en/4015.html>

3.1 Introduction

In this study, we are aiming to demonstrate the experimental generation of radially symmetric Airy beams, using a spatial light modulator and a Fourier transform approach, and finally take advantage of the special characteristics that these exotic beams feature, in order to employ them for Multiphoton Polymerization(MPP) by Direct Laser writing . The distinguished properties of these beams combined with the 3D multiphoton polymerization technology, will provide the fabrication of 3D high aspect-ratio micro-structures for various significant applications.

Multi-photon polymerization (MPP) of photosensitive materials allows one to fabricate complicated three-dimensional (3D) microstructures. When fs infrared laser is tightly focused into the volume of a photosensitive resin (which is transparent in the infrared, femtosecond laser pulses can cause MPP and produce structures with sub-micrometers resolution and lower. The high photon density in the focal volume triggers two-photon absorption by initiator molecules and results in the generation of radicals that, in turn, initiate the polymerization of the resin[1].

3.2 Two Photon absorption

There are two types of two-photon absorption: sequential and simultaneous. In the sequential, the absorbing species is excited to a real intermediate state: then a second photon is absorbed. The presence of the intermediate energy state implies that the material absorbs at this specific wavelength; it will therefore be a surface effect and will follow the Beer-Lambert law [2]. The simultaneous absorption, on which the 2PP technique is based, was originally predicted by Göppert-Mayer in 1931 in her doctoral dissertation. It is defined as an absorption event caused by collective action of two or more photons, all of which must be present simultaneously to impart enough energy to drive a transition. In simultaneous absorption, there is no real intermediate energy state i.e. the material is transparent at that wavelength. Instead, there is a virtual intermediate energy state and two photon absorption happens only if another photon arrives within the virtual state lifetime. For this to occur high intensities are

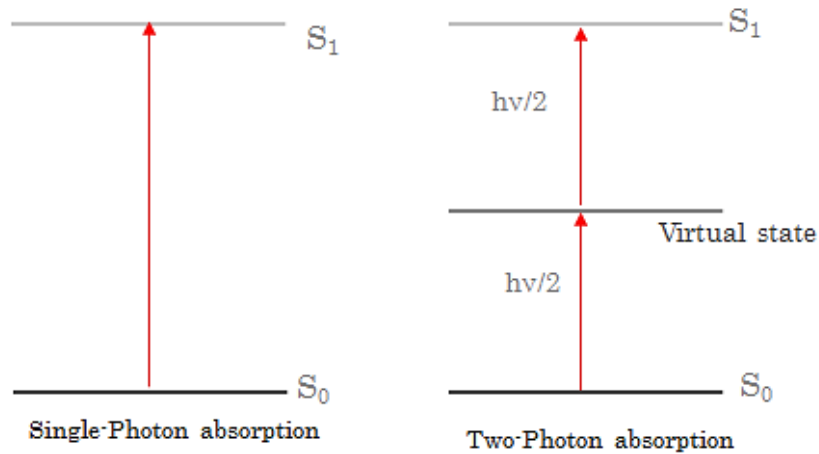


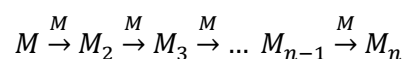
Figure 3.1 | Single Photon and simultaneous Two Photon absorption.

which can only be provided by a tightly focused femtosecond laser beam. The electron transition in this case is caused by two photons of energy $h\nu/2$ rather one of energy $h\nu$. [3] The single Photon absorption and the simultaneous Two Photon absorption are illustrated in Figure 1.

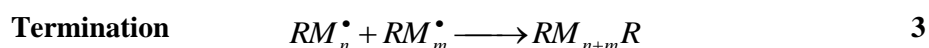
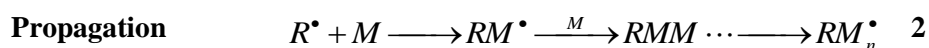
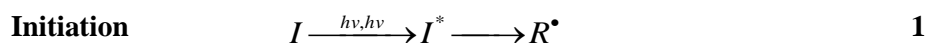
Ti:sapphire lasers are widely used for this purpose. They have two main advantages; firstly they have very short pulses, in the order of a few tens of femtoseconds, so they do not cause thermal damage. Secondly their standard wavelength is 800 nm, which is twice the wavelength of polymerization of a wide range of photopolymers. In addition, most photopolymers are transparent at 800 nm, which allows in-volume focusing of the laser beam with minimal scattering.

3.3 Photo-polymerization

Photopolymerization refers to the process of using light as an energy source to induce the conversion of small unsaturated molecules in the liquid state to solid macromolecules through polymerization reactions. Upon light excitation, the monomers may be solidified by two means: polymerization and crosslinking. An important feature of polymerization is the chain reaction by which macromolecules are created, while cross-linking is concerned more with the formation of crosslinks with chemical bonds. Polymerization, is realized via chain reactions as shown in the following equation:



here M is monomer unit and M_n the macromolecule containing n – monomer units. For practical photopolymer systems, more components are included, most importantly photoinitiators. In order to increase initiating efficiency, one or several low-weight molecules that are more sensitive to light irradiation are added. They form initiating species of radicals or cations by absorbing photons. Such small molecules called photoinitiators. When the laser is focused tightly into the material, the photoinitiator used to initiate the polymerization will absorb two photons and produce radicals. As the material response is proportional to the square of the intensity, this will only happen at the focal point, which, combined with the fact that the two-photon transition rate is very small, will provide very high spatial resolution. The produced radicals will react with monomers or oligomers to produce radical monomers. The process can be described briefly in equations (1-3), which describe the interaction of the initiator (I), the radical (R) and the monomer (M). I^* is the excited state of the photoinitiator, after absorbing the two photons.



This chain reaction will propagate until two radicals meet, and the reaction terminates. An effective initiator has a high quantum yield in the generation of the active moieties, high thermal stability and stability in darkness and is highly soluble in the polymerization medium. Free-radical polymerizations are chain reactions in which the addition of a monomer molecule to an active chain-end regenerates the active site at the chain-end. The free-radical photopolymerization mechanism involves at least three different kinds of reactions [4-5]:

- The first step is the initiation during which the free-radical initiator is decomposed with light in the presence of a monomer to form an active species (eq.1)
- In the next step, known as the propagation, the initiator fragment reacts with a monomer molecule to form the first active adduct that is capable of being polymerized. Monomers continue to add in the same manner resulting in the formation of macro-radicals which are end-active polymers (eq.2).
- The final step is the termination during which the growth is deactivated and the final polymer molecules are formed. This step normally involves the reaction between two polymers bearing active centers and can proceed by two different mechanisms, combination or disproportionation, leading to the formation of one or two polymer chains, respectively (eq.3)

Besides the above, other reactions, such as chain transfer and chain inhibition, often take place and complicate the mechanism of free-radical polymerization.

The diffraction limit: Theoretically, the highest resolution that can be achieved by a focused laser beam is given by Abbe's diffraction limit

$$\frac{0.5\lambda}{N.A.}$$

where λ is the laser wavelength and N.A. is the Numerical aperture of the focusing objective; this has fuelled the race for ever decreasing wavelengths. To produce 3D structures with in-volume patterning, and produce photopolymerized voxels smaller than that defined by the diffraction limit, materials with well-defined photopolymerization threshold need to be used. As the photoinitiator is excited by the laser process, it produces radicals; these radicals are quenched by the oxygen in the system. Quenching is a competing effect to photopolymerization and is usually considered detrimental to the process. In MPP, however, it can be used to circumvent the diffraction limit and produce structures of very high resolution. This can be done by modifying the light intensity at the focal volume, in a manner so that the light-produced radicals exceed the quenching oxygen and initiate polymerization only at a region where exposure energy is larger than the threshold. In this case the diffraction limit becomes just a measure of the focal spot size and it does not really determine the voxel size [3].

Two-photon polymerization, as currently the only micro-processing approach that has intrinsic 3D fabrication capability, has been successfully employed to production of a variety of photonic and micromechanical devices.

The two-photon process [6-8] has at least two advantages compared to single-photon absorption used in conventional rapid prototyping:

1. Common polymers have negligible linear absorption in the red-near-infrared region, so the laser penetrates deeply into materials and directly induces polymerization from inside without contaminating outside of the focal volume. (Figure 2)
2. The quadratic dependence of polymerization rate on the light intensity enables 3D spatial resolution and accuracy is better than that achieved in single photon. (Figure 2)

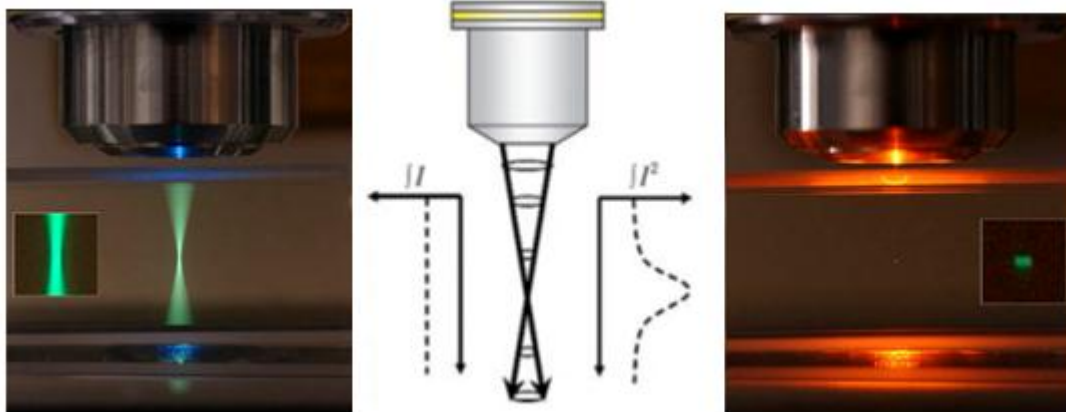


Figure 3.2| Fluorescence from a photopolymer solution, caused by single-photon excitation from a UV lamp (left) and by two-photon excitation from a Ti:sapphire laser operating at a wavelength of 800 nm (right). The integrated intensity in each transverse section of the beam does not depend upon position for single-photon excitation, but is tightly peaked in the focal region for two-photon excitation [9].

Also in order to take advantage of this nonlinear effect (MPP) the use of ultrashort laser excitation is essential. First, a femtosecond laser carries much greater peak power. Multiphoton absorption has an extremely small cross-section; it is confined to occur only in a small 3D volume around the close vicinity of the laser focus, less than the cubic wavelength (λ^3). Hence, a quite high 3D spatial resolution can be achieved in the pinpoint exposure. Secondly, when materials are irradiated with a femtosecond laser pulse, the photon energy is deposited much faster than electrons could transfer it to the lattice, or molecule/atom oscillations through phonon emission, meaning that the excitation is a heat insulation process. This provides an ideal optical excitation means for many photochemical or photophysical reactions where thermal effects, a process difficult to localize, are not desired. In addition, for many dielectric materials, there is a transparent window in the red-NIR spectral region, which is covered neither by electronic band-band absorption nor by atomic/molecular oscillation absorption [1].

3.4 Materials for Laser Polymerization

A composite suitable for 3D structuring by nonlinear Multi Photon Polymerization (MPP) must contain at least two basic components : a polymerizable material, which will become the structure backbone ,and a photo-initiator ,which will absorb the laser light and provide the active species. To date, a large combination of polymeric materials and photoinitiator combinations have been used for this purpose. These are mostly photoresists such as acrylate

materials (and their mixtures), the epoxy-based photoresists SU-8 , and hybrid sol-gel materials .There also a few examples of positive resists being used.

This thesis will mainly focus on hybrid sol-gel materials. Hybrid (organic – inorganic) materials are very popular class of photosensitive materials, as they are easy to prepare, modify and photopolymerize; and after polymerization , they are optically, mechanically and chemically stable. As a result, they have found many applications in 3D photonic and biomedical devices. [10,11] In addition, hybrid materials chemistry provides the possibility of the inclusion of functional groups , such as nonlinear optical molecules and quantum dots.[12,13]

Photoinitiator:

When photo-polymerization take place, a liquid or state monomer is converted into a solid state polymer; this transformation is induced by light. To be attainable MPP into the volume of the material, three conditions must be applied: 1. Both the photo-initiator and the monomer material need to be transparent at the employed laser wavelength, so to allow the laser beam transmission and its penetration to in-volume focusing, 2. The monomer needs to be transparent at the two-photon (or multi-photon) absorption wavelength to avoid thermal damage or ablation, 3. The photoinitiator needs not only to absorb at the two photon (or multi-photon) wavelength, but also to have a high probability to absorb two-photons (or multi-photons) and generate active species; in other words to have a high two-photon (or multi-photon) absorption cross-section. Radical initiators create free radicals which initiate the polymerization process of acrylates. The most commonly used free radical photoinitiator are the benzophenone and its derivatives and consists an effective multi-photon initiator having a high quantum yield in the generation of the active moieties .Also is highly soluble in the polymerization medium.

Polymerizable hybrid materials:

Over the last few years, 2PP research has focused on photosensitive sol–gel hybrid materials [14]. The sol-gel process is a wet-chemical technique, in which the sol (or solution) evolves gradually towards the formation of a gel-like network containing both a liquid phase and a solid phase. Typical precursors are Materials for Laser Polymerization metal alkoxides and metal oxides, which undergo hydrolysis and condensation reactions. The condensation of the hydrolyzed products and other sol–gel-active components present in the reaction medium to form a macromolecular hybrid network structure. The gel formed is subsequently reacted through photo-polymerization to give a product similar to glass.

3D structure fabrication generally involves a four step process (Figure 3.3):

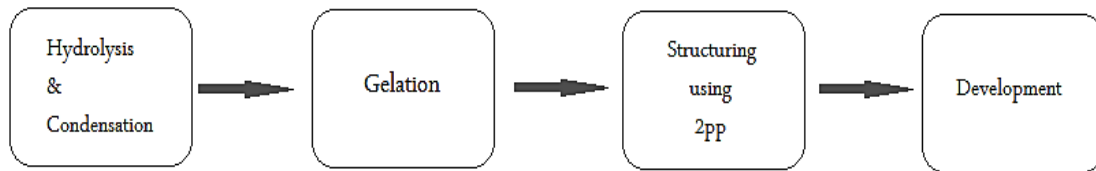
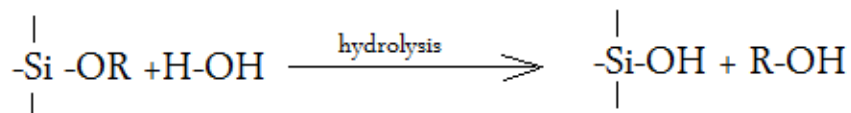


Figure 3.3| 3D structure fabrication generally involves a four step process

At the first step, ‘Hydrolysis & Condensation’, precursors or monomers such as metal oxides or metal alkoxides, are mixed with water and then undergo hydrolysis and condensation to form a porous interconnected cluster structure. An acid such as HCl can be employed as the catalyst:



During the next step, Gelation, the solvent is removed and a gel is formed by heating at low temperature. It is at this stage that solvents are removed and any significant volume loss occurs:



The third step of the process is the photopolymerization. Because of the presence of double bonds, and provided a photoinitiator is present in the gel, the induced radicals will cause the polymerization of the unsaturated moieties only in the area the radicals are produced. At this step there is no material removal and no volume loss; the only reaction is the addition of the monomers to the active center. The last step is the development; the sample is immersed in an appropriate solvent and the area of the sample that is not photo-polymerized is removed. Figure 3.4 shows a 3D photonic crystal structure fabricated using multiphoton polymerization by direct laser writing and the sol-gel chemical technique.

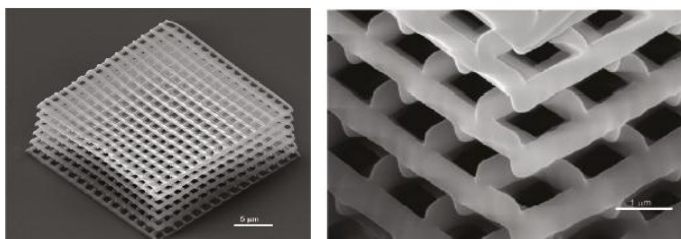


Figure 3.4| SEM images of representative woodpile structures made of Zr-based hybrid photosensitive materials [15]

References

1. Sun H-B and Kawata S Springer-Verlag 2004. *Two-photon Photopolymerization and 3D Lithographic Microfabrication*
2. Jacobs P F.1992 *Rapid Phototyping and manufacturing: Fundamentals of stereolithography* (Deaborn ,MI: society of Manufacturing Engineers)
3. Maria Farsari, Maria Vamvakaki and Boris N Chichkov , *Multiphoton polymerization of hybrid materials*, 2010 IOP Publishing Ltd
4. Stevens M P 1999 , *Polychemistry: An introduction* (New York :Oxford University Press)
5. Allcock H R , Lampe F W and Mark J E 2003 *Contemporary Polymer Chemistry* (Upper –Saddle River .NJ: Pearson- Prentice –Hall)
6. FarsariM, Filippidis G and Fotakis C 2005 *Fabrication of three-dimensional structures by three-photon polymerization* Opt. Lett. 30 3180–2
7. Jun Y, Nagpal P and Norris D J 2008 *Thermally stable organic–inorganic hybrid photoresists for fabrication of photonic band gap structures with direct laser writing* Adv. Mater. 20 606–10
8. Manhart J, Kunzelmann K H, Chen H Y and Hickel R 2000 *Mechanical properties of new composite restorative materials* J. Biomed. Mater. Res. 53 353–61
9. (Image by Steve Ruzin and Holly Aaron, UC Berkeley)
10. Farsari, M.; Vamvakaki, M.; Chichkov, B. N., *Multiphoton polymerization of hybrid materials*. J.Opt. 2010, 12, (12), 124001
11. Schizas, C.; Melissinaki, V.; Gaidukeviciute, A.; Reinhardt, C.; Ohrt, C.; Dedoussis, V.; Chichkov, B. N.; Fotakis, C.; Farsari, M.; Karalekas, D., *On the design and fabrication by two-photon polymerization of a readily assembled micro-valve*. Int.J.Adv.Manuf.Technol. 2010, 48, (5-8), 435-441.
12. Farsari, M.; Ovsianikov, A.; Vamvakaki, M.; Sakellari, I.; Gray, D.; Chichkov, B. N.; Fotakis, C., *Fabrication of three-dimensional photonic crystal structures containing an active nonlinear optical chromophore*. Appl.Phys.A 2008, 93, (1), 11-15.
13. Jia, B.; Buso, D.; Embden, J. v.; Li, J.; Gu, M., *Highly Non-Linear Quantum Dot Doped Nanocomposites for Functional Three-Dimensional Structures Generated by Two-Photon Polymerization*. Adv. Mater. 2010, 22, 2463–2467.

14. Penard A L, Gacoin T and Boilot J P 2007 *Functionalized sol-gel coatings for optical applications* Acc. Chem. Res. 40 895–902
15. Sakellari et al., *Diffusion-Assisted High-Resolution Direct Femtosecond Laser Writing*, ACSNANO, 2012, vol.6,NO.3,2302-2311

PART II - EXPERIMENTAL DEMONSTRATION

4.1 Introduction

In this dissertation we are focusing on the experimental realization of radially symmetric Airy beams or ring Airy-beams which tend to abruptly autofocus. They also present long working distances, tight focusing and small focal volumes [1]. We want to show their tunability and the methods to control their characteristics and dynamics. In particular, in chapter four we demonstrate the experimental generation of ring-Airy beams, using a spatial light modulator and a Fourier transform approach. We spatially control the autofocus position of these beams and we show that the focus, at which an abrupt increase of intensity is observed, can be shifted along the propagation axis. Furthermore, we investigate the dimensions and shape of the focal volume (voxel) and how we manipulate the working distance of the ring-Airy beam. Theoretical calculations and comparison with Bessel beams will be mentioned too.

4.2 Experimental demonstration

To explore the propagation dynamics and spatial manipulation of ring-Airy beams, we experimentally generate them using a Fourier Transform (FT) approach, described in detail in ref. 1. The radially symmetric Airy distribution can be generated using the FT of a properly modulated input wave. In particular, a Gaussian beam is modulated by a cubic phase; and the FT of the ring-Airy beam is a Bessel-like distribution with a central peak which is surrounded by decaying amplitude rings. Figure 4.1(a) shows the experimental set-up for the ring-Airy beam generation. A Hamamatsu LCOS-X10468-2 phase reflecting only spatial light modulator (SLM) is employed for the phase modulation of a Gaussian beam which is then Fourier transformed by a lens (FT lens, 400mm). The FT of the radially symmetric Airy distribution is encoded onto a phase filter applied onto the spatial light modulator (SLM) and the ring-Airy distribution is generated at the Fourier transform plane (FT plane) of the FT lens after blocking the zero-order diffraction. The further reduction of the effective focal length of the generated ring-Airy beam is achieved using a 4f optical system composed by a 200-mm lens and a 3.7x microscope objective. A Ti:Sapphire femtosecond laser (800nm, 50Hz, 35fs)

was used as a light source. The autofocusing property of the generated ring-Airy beams was easily observed using a compact microscope system and a linear - charge - coupled device

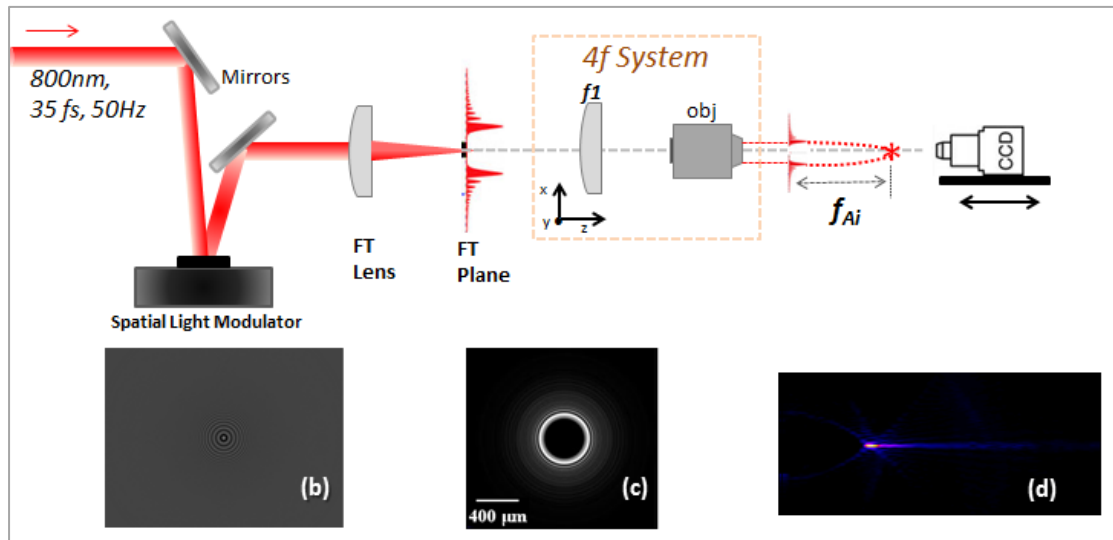


Figure 4.1(a) Experimental setup. FT lens(400mm); f_1 (200mm); Obj (microscope objective x3.7); f_{Ai} : effective focal length of the ring-Airy (b) typical used phase mask (c) experimental intensity profile as captures by the CCD at the Fourier Transform plane (blocked zero order) (d) typical experimental demonstration of a ring-Airy beam propagation dynamics.

camera (14bit, 800x600 pixels). Figure 4.1(b) shows a 2D phase mask used for phase modulation of the Gaussian beam, while Figure 4.1(c) shows a typical experimental intensity profile at the FT plane (blocked zero order). It corresponds to the primary ring distribution as captured by the CCD camera at the FT plane of the FT lens. Secondary and lower intensity concentric rings of the ring-Airy distribution are visible too. A ring-Airy beam propagating over z-axis can be seen in Figure 4.1(d), as captured by the CCD.

4.3 Ring-Airy beam Manipulation – Working distance Control

Ring-Airy beams belong to a new class of optical beams that, due to their phase and amplitude distribution, are able to abruptly autofocus. In contrast to typical focusing, where the spot size shrinks linearly as we approach the focus, these beams exhibit a non-linear, power law, shrinking of the spot size. This enables them to exhibit a sudden, orders of magnitude increase of the intensity at the focus even at long

working distances. Ring–Airy beams are actually cylindrically symmetric Airy beams [2,3] with their distribution described by [1,5,11]:

$$u_o(r,0) = Ai\left(\frac{r_o - r}{w}\right) \exp\left[\alpha \cdot \left(\frac{r_o - r}{w}\right)\right], \quad (1)$$

where $Ai(\cdot)$ denotes the Airy function, r is the radius, r_o is the radius of the primary ring, w is a scaling factor and α an exponential decay factor. The radius of the primary ring is given by $R(0) \cong (r_o + w)$ while its full width at half maximum (FWHM) is $\cong 2.28w$ [5]. As it propagates, the beam autofocuses following a parabolic trajectory [1] at a distance f_{Ai} defined as effective focal length, which at low input powers [1,5] is described by:

$$f_{Ai} = \frac{4\pi}{\lambda} w^{3/2} R_0^{1/2} \quad (2)$$

It is clear from eq. 2 that the focus position of a ring-Airy beam can be tailored by properly tuning the w and r_o parameters. ***Consequently, the focal distance of the abruptly autofocusing beams can be controlled by the initial size of the primary Airy ring, its radius r_o and width w .*** It is, therefore, conceivable that the use of such beams in MPP would allow the significant increase of the height of structures. For this reason, various ring-Airy beam distributions were experimentally generated by applying the appropriate phase mask onto the SLM in order to show the focus distance control of these beams. Two design strategies were studied in detail: ring-Airy beams with constant primary ring radius ($r_o=162 \mu\text{m}$) but different ring widths and ring-Airy beams with constant ring width ($w=19 \mu\text{m}$) and variable ring radius. In both strategies the focus position and thus the working distance is manipulated, although the focus characteristics differ. By adjusting the radius r_o or the width w in the encoded phase mask holograph, the working distance manipulation was achieved. The intensity profiles of some of the experimentally generated ring-Airy beams, as captured by the CCD at the FT plane (blocked zero order) are shown in Figure 4.2. It is observed that the central and highest intensity concentric ring vary in size for each ring-Airy beam.

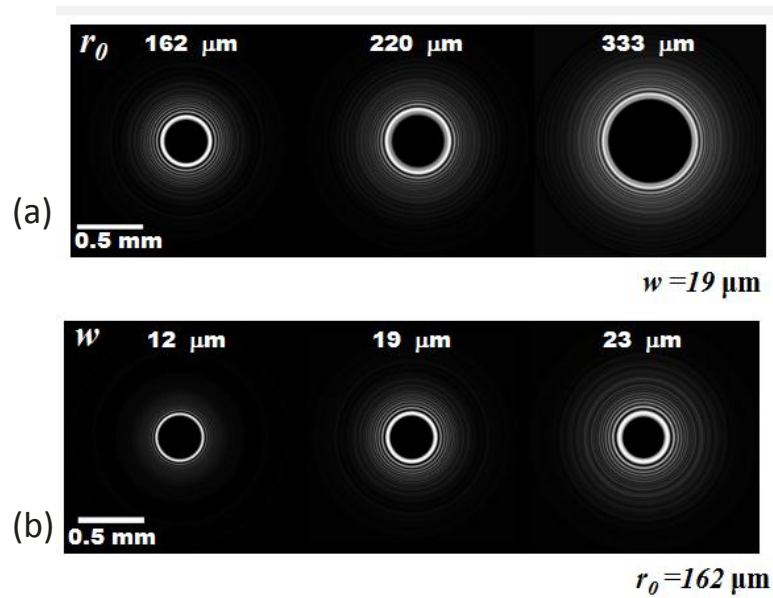


Figure 4.2| Primary ring Airy profiles at the plane of generation: Experimental, radially averaged, intensity profiles of the generated ring-Airy beams as captured by the CCD at the Fourier Transform plane (blocked zero order); (a) three different primary ring intensity distributions of varying r_0 (b) three different primary ring intensity distributions of varying widths w .

In Figure 4.3 the normalized intensity distributions along the propagation axis for each of the experimentally generated ring-Airy beams presented in Figure 4.2, are shown. It can be seen that the peak intensity position of each ring-Airy beam shifts to various focus positions, covering a long range over the z propagation axis. The asymmetric intensity profile before and after the focus, and the abrupt intensity increase near the focus, typical characteristics of the abruptly autofocusing beams [1,10] is clearly visible, independently of the focus position. Furthermore, although the focus shifts, covering an extended range over the propagation axis, the intensity distribution in the focal area is practically the same. This is a clear demonstration of the capability of such beams to deliver. *The focal distance therefore can be controlled by the initial size of the primary Airy ring at the plane of generation.* In addition, the beam intensity is very low before and after the focus position, while it is abruptly increased at the focus, confirming the autofocusing property of these beams.

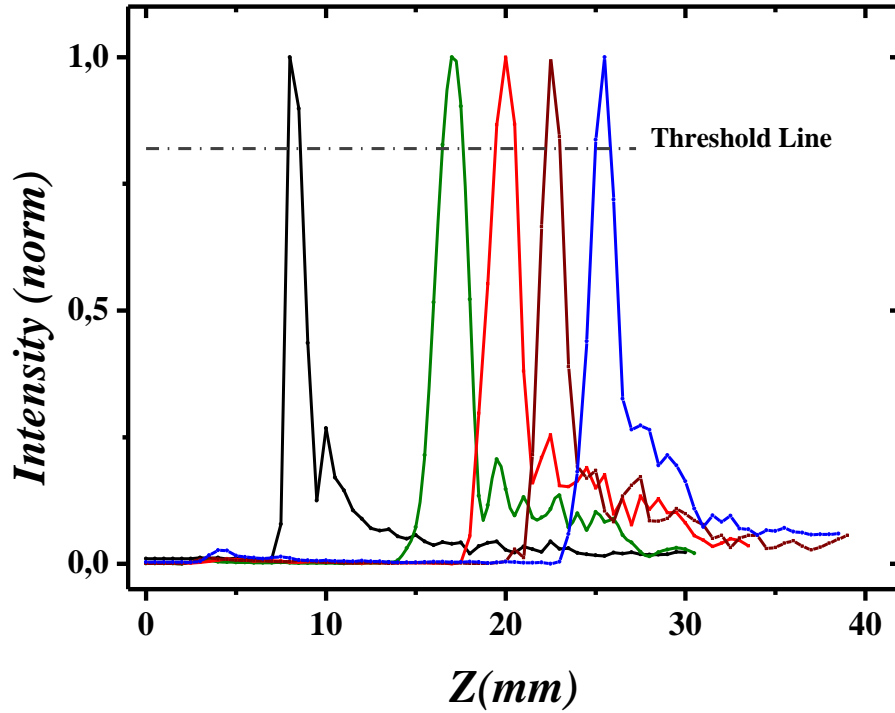


Figure 4.3| Experimental Intensity profiles: Experimental intensity distribution (normalized values) of the ring-Airy beams along the propagation axis. *Normalization: intensity values are normalized to the peak intensity I_{max} at the focus position of each ring-Airy beam.*

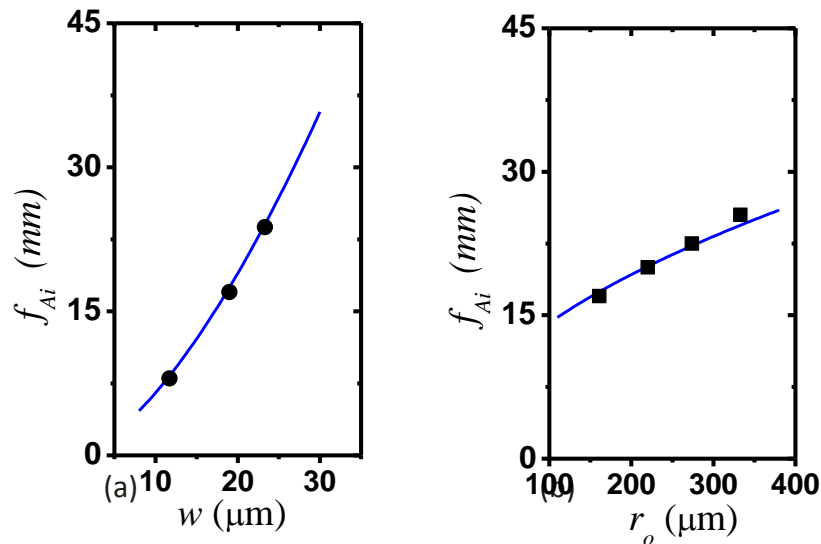


Figure 4.4| Focus position control: (a) Focus shift for ring - Airy Beams with primary ring radius $r_0 = 162\mu\text{m}$, as a function of different widths at the FT plane, (b) Focus shift as a function of radius r_0 , for ring - Airy beams having equal primary ring widths ($w=19\mu\text{m}$) at $z=0\text{mm}$ position. (\bullet, \blacksquare)Experimental points, (blue line) theoretical simulation.

As mentioned, we can spatially control the effective focal distance (f_{Ai}) of the generated ring-Airy beam by tuning the dimensions of the primary ring. Figure 4.4 analytically describes the effect of radius and width change on the focal position control. The theoretical curves are calculated using eq. 2. By increasing the radius r_0 , the focal position can be controlled in almost linear fashion (Figure 4.4(a)). Ring-Airy beams having similar radius r_0 , present a focus position shifting, by increasing the w parameter. There is a satisfying agreement between the experimental points and the theoretical curve (continuous line), for both Figures 4.4(a) and 4.4(b). Therefore, the working distance of the ring-Airy can be accurately controlled to cover an extended range by using the theoretical predictions of eq. 2.

4.4 The ring-Airy focal Voxel: dimensions and shape

The shape and dimensions of the ring-Airy focal volume or voxel are of particular interest. Experimental values about the length and the diameter (spot size) of the focus over the effective focal position measured from the FT plane are shown in Figure 4.5. The shape and dimensions of the focal volume are directly related to the voxel of the MPP process and are of particular interest. The transverse and the longitudinal size of the voxel in the MPP process are correlated respectively to the spot size and the FWHM of the longitudinal intensity distribution of the ring-Airy beam. In the case of ring-Airy beams of varying w and constant $r_0=162\mu\text{m}$ both the voxel width and length are increased as the focus is moved further away. On the other hand, ring-Airy beams with varying r_0 and constant $w=19\mu\text{m}$, present a decrease in width and length (Figure 4.5(a)) as the focus is moved further away. This behavior is expected since the increase of r_0 is effectively similar [1] to the increase of the numerical aperture (or decrease of the f-number) of a typical Gaussian beam. Also, Figure 4.5(b) shows that the diameter of the voxel seems to increase as the ring-Airy beams with $r_0=162\mu\text{m}$ are focused on longer distances measured from the FT plane. But, for ring-Airy beams of $w=19\mu\text{m}$, a spot size reduction is observed as the working distance is longer.

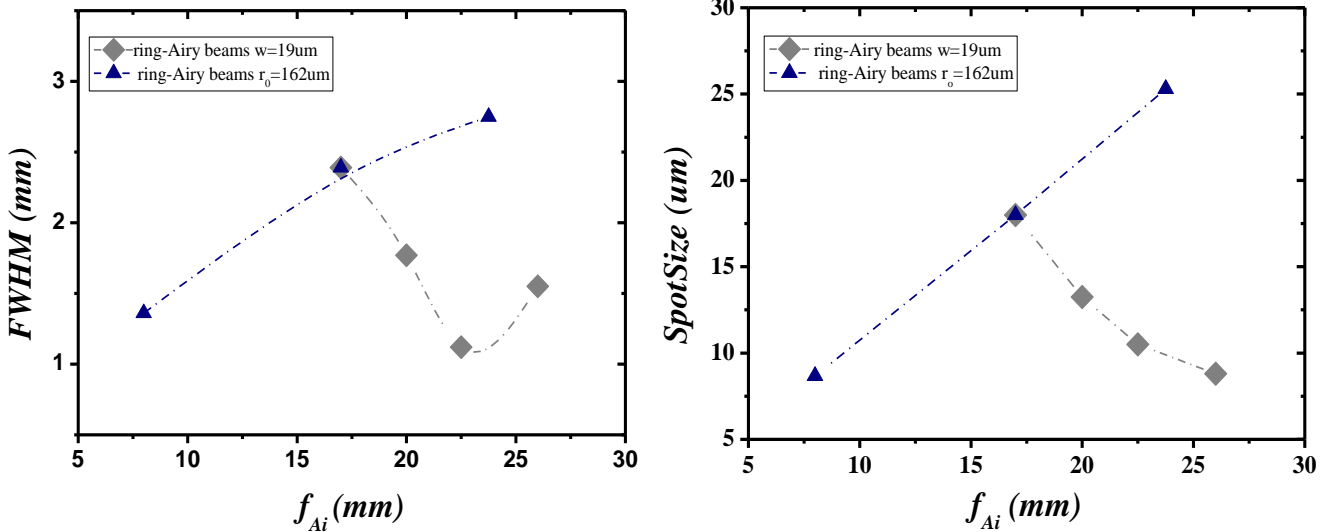


Figure 4.5| Focal volume control: (a) The longitudinal size (FWHM) of the focal voxel as a function of the focus position for the cases of generated ring-airy beams (b) The spot size (radius in μm) of the focus voxel as a function of focus position.

These beams present tight focusing over a long distance, which we can now control. The focal length is now in the millimeter range while the spot size remains at few micrometers. The voxel looks in shape like a long needle with a small diameter. So, a high aspect ratio voxel is achieved, when the beam autofocuses. Therefore, apart from the working distance manipulation, the focal voxel dimensions could be also controlled at the same time.

4.5 Bessel beams and comparison with ring-Airy beams

Clearly the application of ring –Airy beams in MPP results in extended focal range control and needle like voxel structures. Therefore, it is more appropriate to compare them not only with classical Gaussian beams, but also with beams that lead to similar needle-like voxel shapes, such as the Bessel beams. Bessel beams are non-diffracting, and keep their transverse intensity profile invariant along the propagation direction as first suggested and observed by Durnin et al. These beams keep invariant their transverse intensity profile and propagation direction [5,6]. Bessel beams are generated from an appropriate conical superposition of plane waves [5-7]. These beams present properties of great interest, such as the self-healing property according to which they reconstruct when obstructed at some point of propagation. Also, they present tight focusing over a long distance (Bessel zone) [8].

We experimentally and theoretically generate zero-order Bessel beams whose profile consists of a high intensity central lobe surrounded by a series of concentric rings. Bessel beams

consist of a conical wavefront and can be easily generated using an axicon lens (ref. 9). In our case, in order to compare the ring –Airy and Bessel beams under the same conditions we applied an appropriate conical phase filter to the phase SLM (Fig. 1). The required phase to generate a Bessel beam is given by $\varphi(r) = -(2\pi / \lambda) \tan(\gamma) \cdot r$, where r is the radius, λ is the wavelength, γ is the Bessel cone angle. [1] The Bessel zone, i.e. the longitudinal range of the Bessel focus, can be then controlled by masking Bessel beam allowing an annular ring part to propagate. For the experimental realization, an appropriate conical phase filter was applied onto the SLM (Figure 4.6). In Figure 4.6(a) a typical conical phase filter mask for Bessel beam generation is shown. Bessel beams can also be generated using a simple axicon lens (ref 9). By tuning the radius of the annular ring while keeping its width constant, the working distance of the generated Bessel beam can be controlled (Figure 4.7(b)). In Figures 4.6(b), (c), (d) annular clipped conical phase filter masks of various annular ring radii, used for Bessel beam generation and working distance control, are shown. The simulated intensity distributions (normalized values) of the Bessel beams are shown in Figure 4.7(a). The parameters of the beams are selected so that the focus position is the same as in the ring –Airy beams.

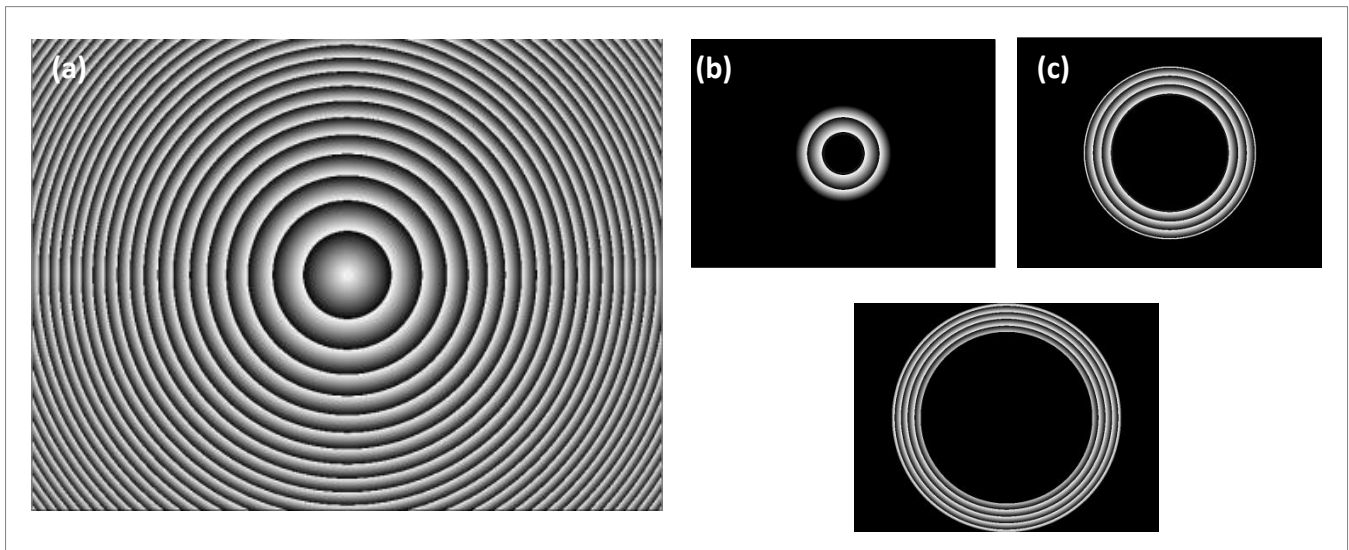


Figure 4.6| Focal volume control: (a) typical conical phase filter mask for Bessel beam generation, (b), (c), (d) annular clipped conical phase filter masks generating by selecting a specific annular ring-part of the 4.5(a) mask, they present annular rings of same width and various radii.

As expected, by the increasing the annular ring clip radius, the focal distance of the Bessel beam also increases. The FWHM of these beams corresponds to the Bessel zone, which in a

MPP application controls the voxel's length. It can be seen that as the Bessel distribution is shifted further away; the Bessel zone becomes longer, affecting the control of the focal voxel dimensions.

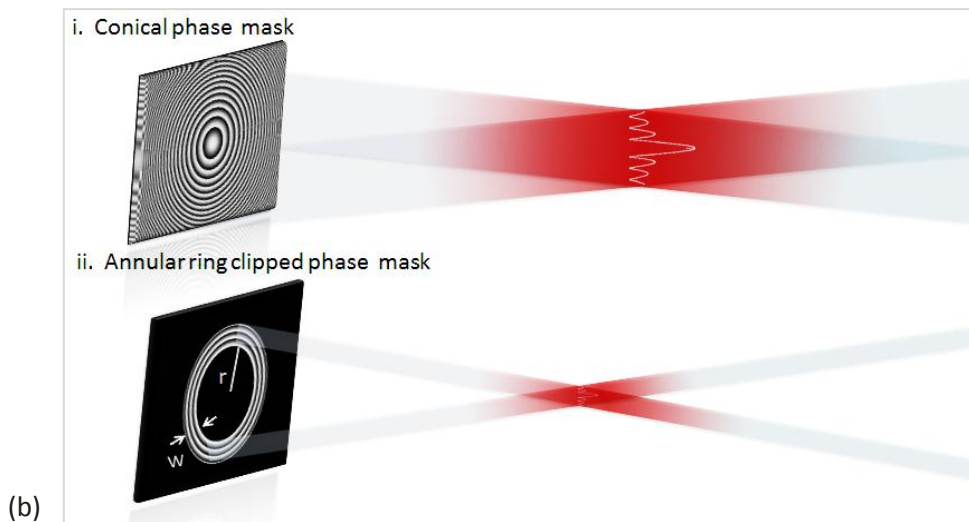
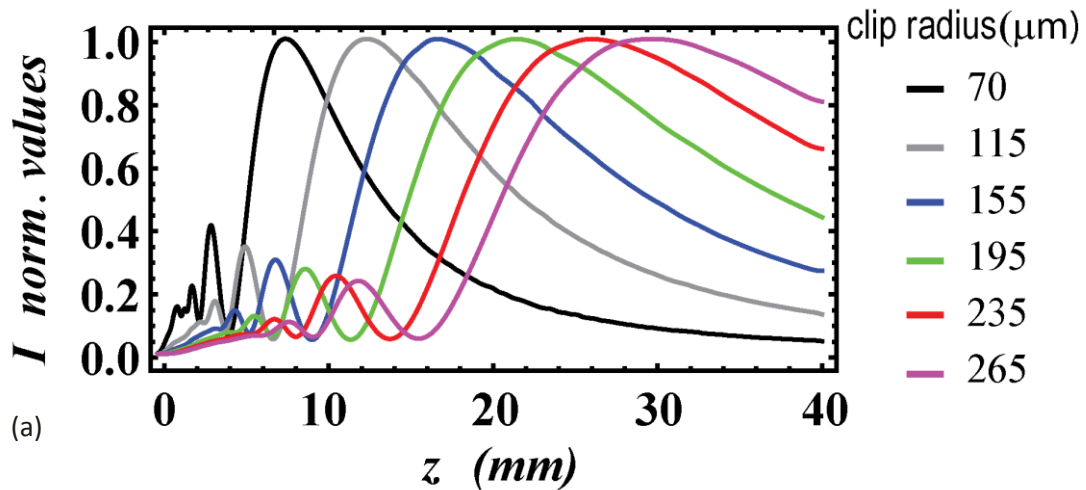


Figure 4.7| Simulation results-Bessel with variable clip radius: (a) Intensity distribution of the Bessel beams versus propagation distance for various clipped annular radius, (b) (i) Conical phase mask generating a Bessel beam, (ii) controlled masking of Bessel beam allowing only an annular ring of radius r and width w , to propagate.

In Figure 4.8 we show comparative simulations of z - y plane intensity profiles, for the propagation of ring-Airy and clipped Bessel beams. The focal volumes are clearly visible for

the three beam examples; two ring-Airy beams tailored by respectively varying the ring width or diameter and an annularly clipped Bessel. For the ring-Airy beams, it is easy to observe the abrupt autofocusing behavior and successful working distance control. The high intensity focal voxels are moved on specific distances with minor variation on their dimensions. In the case of Bessel, although the clipping approach enables the manipulation of the working distance, the focal volume is more dispersed.

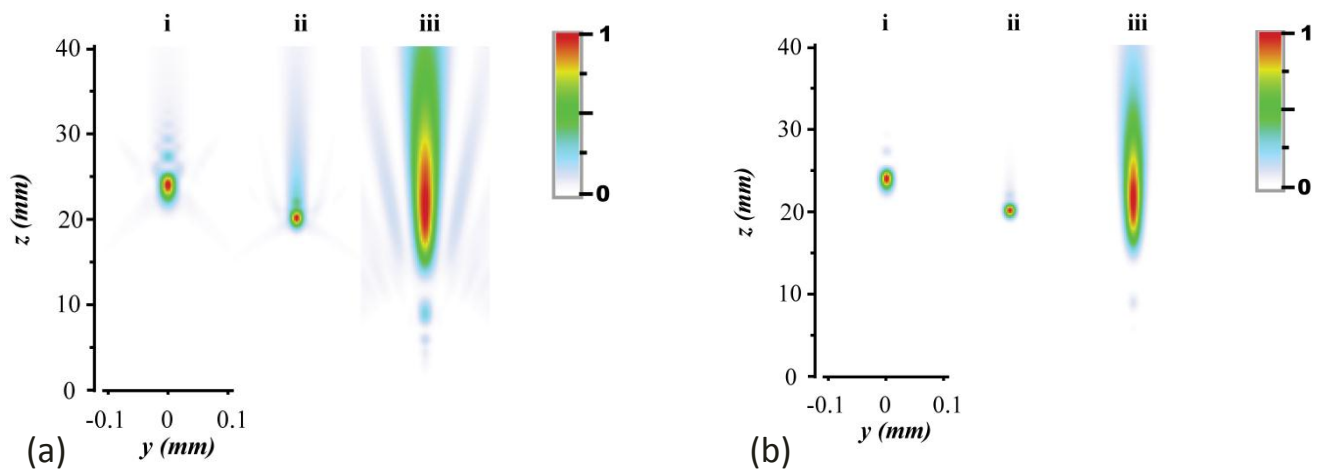


Figure 4.8| Simulation of intensity profiles over propagation: (a) (i) ring Airy focus controlled by varying ring width ($r=162\mu\text{m}$, $w=23\mu\text{m}$), (ii) ring Airy focus controlled by varying ring diameter ($r=220\mu\text{m}$, $w=19\mu\text{m}$), (iii) Bessel clipped by annular ring (clip radius $195\mu\text{m}$);(b) Intensity squared (two photon) profiles over propagation (i) Airy ring focus controlled by varying ring width ($r= 162\mu\text{m}$, $w= 23\mu\text{m}$), (ii) Airy ring focus controlled by varying ring diameter ($r= 220\mu\text{m}$, $w= 19\mu\text{m}$), (iii) Bessel clipped by annular ring (clip radius $195\mu\text{m}$).

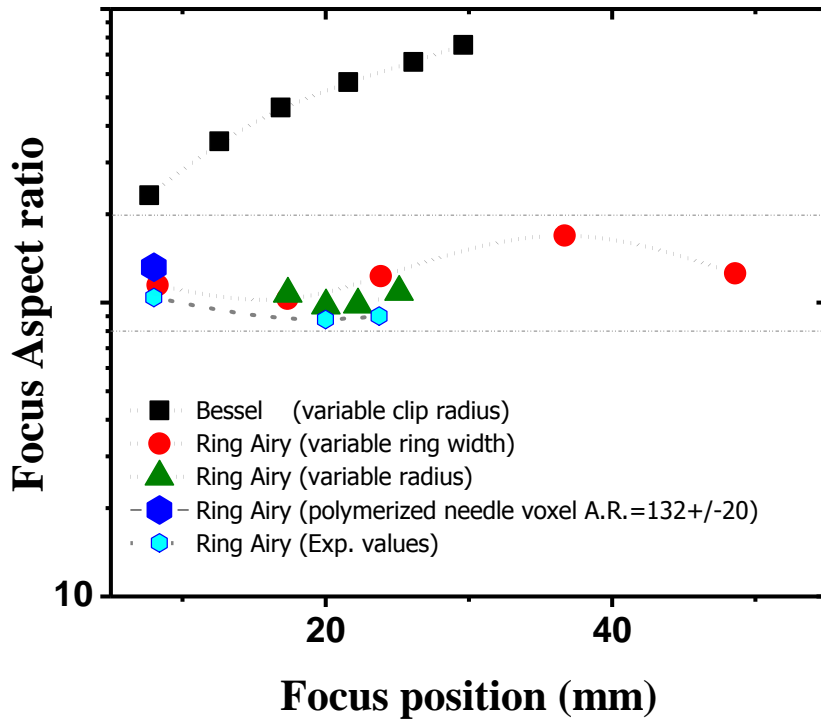


Figure 4.9|Focal voxel aspect Ratio comparative curves: Focal voxel aspect ratios over effective focal length for various experimental and simulated ring Airy and Bessel beams.

One important aspect in the use of such beams in MPP application is the variation of the voxel shape and dimensions as the focus position is optically manipulated along the propagation axis. To better understand the different behavior of each beam we present in Figure 4.9 the focal voxel aspect ratios (AR) as a function of the focal for all studied beams. The AR is defined as the ratio of voxel longitudinal size over its diameter. All the data appeared on Figure 4.9 correspond to the 0.8 threshold of the peak intensity distributions, (threshold line in Figure 4.2). The AR can be estimated from the intensity distribution of the focal volume taking into account that MPP is actually a threshold process. In an MPP application the polymerization takes place only at areas where the intensity I is high enough so that $I^n \geq C$, where n is the order of the multiphoton polymerization process and C a constant. In our estimations we used the 80% of the peak intensity distribution as a threshold (see threshold line in **Error! Reference source not found.**). It is clear that experimentally generated ring-Airy beams controlled by variable ring radius, keep almost invariant the focal aspect ratio. However, the aspect ratio for Bessel beams is variable as the clip radius is

increased. So, the aspect ratio control seems to be more effective for ring-Airy beams. Interestingly, ring-Airy beams, independently of the approach used to manipulate the focus position, keep the voxel aspect ratio almost invariant. On the other hand, the voxel aspect ratio for Bessel beams is increasing as the beam focus is pushed further away.

Concluding this chapter, the autofocusing position of a ring Airy beam is spatially controlled. These tunable beams show a high aspect ratio focal voxel that can be positioned at different working distances with almost invariant dimensions and shape. Apart from the ring-Airy beams, the working distance control of the Bessel beams was also showed to be successfully achieved. In comparison with Bessel beams, the aspect ratio control seems to be more effective for ring-Airy beams. These remarkable properties of ring-Airy beams make them ideal candidates for Direct Laser Writing by Multiphoton Polymerization. This application is extensively discussed in the following Chapter (Ch.5).

References

1. D.G. Papazoglou, N.K. Efremidis, D.N. Christodoulides, S. Tzortzakis, *Opt. Lett.* **36**, 1842 (2011)
2. Siviloglou, G. A. & Christodoulides, D.N. Accelerating finite energy Airy beams. *Opt. Lett.* **32**, 979-981 (2007)
3. Siviloglou, G. A., Broky, J., Dogariu A., & Christodoulides, D.N Observation of accelerating airy beams. *Phys. Rev. Lett.* **99**, 213901 (2007)
4. M.V. Berry, N.L. Balazs, *Am. J. Phys.* **47**, 264 (1979)
5. Panagiotopoulos, P., D. G. Papazoglou, et al. (2013). "Sharply autofocused ring-Airy beams transforming into non-linear intense light bullets." *Nat Commun* **4**: 2622
6. J. Durnin, *J. Opt. Soc. Am. A* **4**, 651 (1987)
7. J. Durnin, J.J. Miceli, J.H. Eberly, *Phys. Rev. Lett.* **58**, 1499 (1987)
8. D. McGloin, K. Dholakia, *Contemp. Phys.* **46**, 15 (2005)
9. K.Dholakia and T.Cizmar , *Nature Photonics* doi: 10.1038/nphoton.2011.80
10. Liang Yang et al., Two-photon polymerization of cylinder microstructures by femtosecond Bessel beams *Appl. Phys. Lett.* **105**, 041110 (2014)
11. Efremidis, N. K. and D. N. Christodoulides (2010). "Abruptly autofocusing waves." *Opt. Lett.* **35**(23): 4045-4047.
12. Suntsov, S., D. Abdollahpour, et al. (2013). "Tailoring femtosecond laser pulse filamentation using plasma photonic lattices." *Applied Physics Letters* **103**(2): 021106-021103.

5.1 Introduction

Direct Laser Writing (DLW) by Multi-Photon Polymerisation (MPP) is an established technique for the three-dimensional (3D) printing of mm-scale structures with tens of nanometers (nm) resolution [1, 2]. In DLW, the beam of an ultrafast laser is tightly focused into the volume of a photopolymer. Polymerization is initiated by multi-photon absorption within the volume element-the voxel. Scanning the voxel in a three-dimensional manner, one can obtain arbitrary 3D structures.

To obtain the small voxel, and therefore the sub-100 nm resolution, high numerical aperture (N.A.) microscope objectives are employed for focusing the laser beam. These objectives, however, have the disadvantage of short working distance, which limits the height of the fabricated structures. For example, a typical 100x, 1.4 N.A. oil-immersed objective has a working distance of 170 microns. If one takes into account that, in order to avoid contact between the oil and the photopolymer, the material has to be back-illuminated through a glass substrate typically 100 microns thick, this reduces the maximum height of the structure to 70 microns.

To address this issue, “Dip-in” Lithography [3] and the similar WOW-2PP [4] were developed, where the microscope objective is immersed into a liquid photopolymer. In the first case the photopolymer has a refractive index matching that of the objective, while in the second case the objective is encaged in a protective case, so that it doesn’t have direct contact with the photopolymer. This way and with both techniques, the working distance becomes an irrelevant factor. While this approach somehow solves the problem, however, it also has limitations. “Dip-in” Lithography only works with one specific photopolymer, whose index is matched to the objective. WOW-2PP also only works with liquids, while the most popular MPP materials are SU8 and hybrid materials, both solids.

Here, we propose an alternative method to overcome the short structure height problem, by employing non-diffracting radially symmetric Airy beams. We have already show in the Chapter four, that these beams present notable characteristics like their autofocusing feature while we demonstrated that we can completely control their propagation dynamics. We spatially control the effective focal distance (f_{Ai}) of the experimental generated ring- Airy beam by tuning the size of the primary ring at the FT plane. Therefore, we can manipulate the

working distance of the optical system that these beams are introduced. Moreover, these tunable beams show a high aspect ratio focal voxel that can be positioned at different working distances with almost invariant dimensions and shape. The controllable, long working distance and the high aspect ratio focal volume, surpass the restrictions set to the overall height of a 3D structure when using Gaussian beams and small working distance, high NA objective lenses. In this Chapter, we show some of the structures made by ring-Airy beam induced MPP and prove that the use of such beams in MPP would allow the significant increase of the height of structures, important for various applications.

5.2 Set-up for MPP by ring-Airy beams

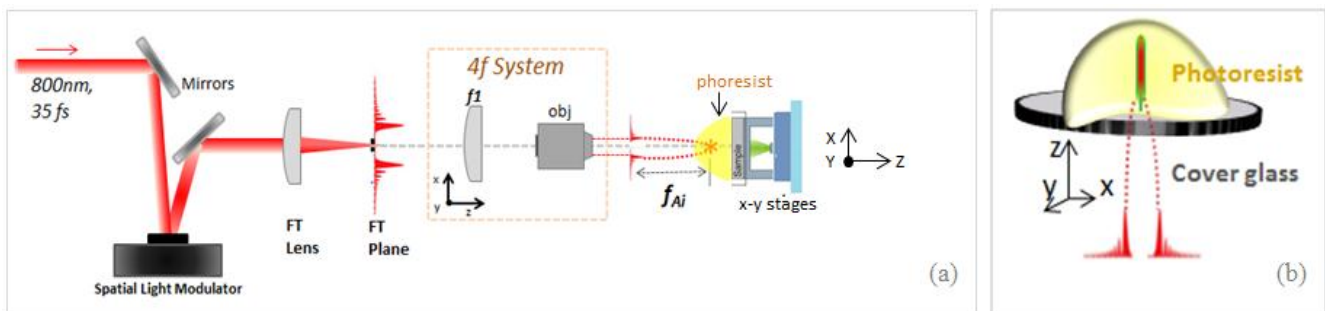


Figure 5.1(a) Experimental setup. FT lens(400mm); f_1 (200mm); Obj (microscope objective x3.7); f_{Ai} : effective focal length of the ring-Airy (b) ring-Airy beam propagation; the beam is let to autofocus inside the volume of the photoresist in order multiphoton polymerization to be induced.

The experimental set-up used to induce MPP by ring-Airy beams for the construction of 3D structures is described in Figure 5.1(a). A Ti:Sapphire femtosecond laser (800nm, 50Hz, 35fs) was used as light source. The Gaussian beam is modulated by a cubic phase by a Hamamatsu LCOS-X10468-2 phase reflecting only spatial light modulator. The ring-Airy distribution is generated at the Fourier transform plane (FT plane) of the FT lens after blocking the zero-order diffraction. The further reduction of the effective focal length of the generated ring-Airy beam is achieved using a 4f optical system composed by a 200-mm lens and a 3.7x microscope objective. The ring-Airy laser beam was generated to autofocus into a photosensitive composite (Figure 5.1(b)). The photo-sensitive composite samples were prepared by drop-casting onto 100 μm thick salinized glass substrates and were mounted on

x-y stages for point by point movement. The ring-Airy beam was autofocused inside the volume of the photoresist while propagating over z-axis; and by moving the sample on x-y axis using computer-controlled stepper motors, the in-volume patterning was achieved.

5.3 Photosensitive material for MPP by ring-Airy beam

The material used for the fabrication of the three dimensional structure using a ring-Airy beams is a zirconium-silicon organic-inorganic material doped with tertiary amine metal binding moieties. [1] Hybrid materials (organic – inorganic) are a very popular class of photosensitive materials , as they are easy to prepare , modify and photopolymerize and , after polymerization , they are optically ,mechanically and chemically stable. As a result, they can find application in various 3D photonic and biomedical devices.

The main materials used here for the synthesis of the photopolymer were methacryloxy-propyltrimethoxysilane (MAPTMS ,99%), and zirconium n-propoxide (ZPO) 70% solution in 1-propanol. This hybrid organic-inorganic, zirconium-propoxide doped photopolymerizable material was prepared as described in [5] and the sol-gel process was used for the composition. MAPTMS was firstly hydrolyzed by adding HCL (0.1 M) at 1:0.1 ratio and the mixture was stirred till the mixture becomes transparent again. The molar ratios were 8:2 for MAPTMS/ZPO. Next, ZPO was mixed with MAA (methacrylate acid) and the mixture was stirred for 15 minutes. Finally , the photoinitiator 4,4-bis(diethylamino) benzophenone (agent which initiates the polymerization process of acrylates , absorbing the laser light and providing active species) was added at a 1%w/w concentration to the final solution. The solution was filtered using 0.2 μm syringe filters. The chemicals used for the photosensitive composite synthesis are illustrated in Figure 5.2. Before structuring, the samples were prepared by drop-casting onto 100 μm thick silanized glass substrates , and the resultant films were dried in an oven at 50 $^{\circ}\text{C}$ for 10 min before the photopolymerization or left at room temperature overnight. During this step, Gelation , the solvent is removed and a gel is formed. The glass substrates were first treated in dichromethane/MAPTMS solution (20ml CH_2Cl_2 – 250 μl MAPTMS), and after this treatment a small droplet of the hybrid material was placed on the top of the glass. The heating process led to the condensation of the alkoxide groups and

the formation of the inorganic matrix. Next, the organic moieties can be polymerized using DLW (Direct Laser Writing), resulting in the formation of irreversible and fully saturated aliphatic C-C covalent bonds that further increase the connectivity of the material. After the completion of the component build process by DLW, the samples are developed for 20 min in a 70:30 solution of 2-propanol/1-propanol and the area of the sample that was not photopolymerized was removed. The structure fabrication process by MPP generally involves the four steps described in Figure 5.3.

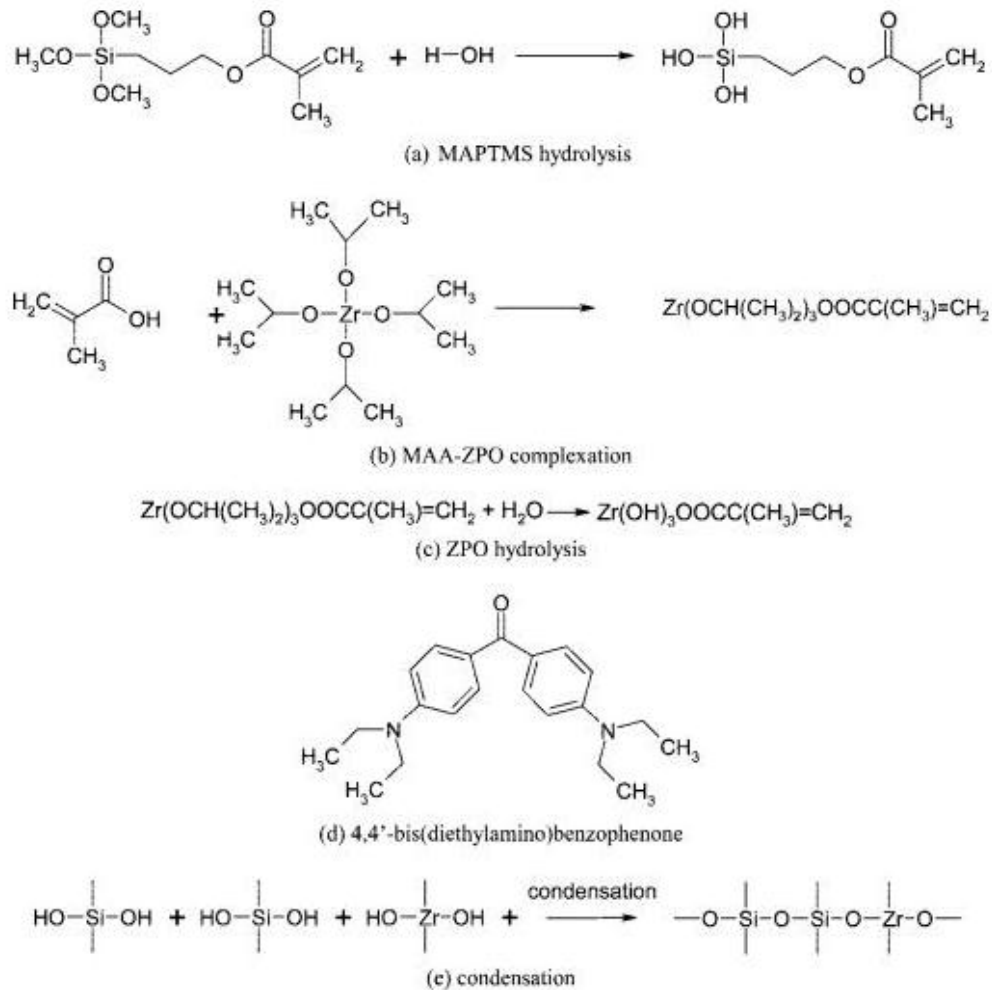


Figure 5.2| Chemical structures of the reagents used for the hybrid material synthesis and sol-gel process.



Figure 5.3| MPP four step process for structure fabrication

5.4 3D structures fabricated by ring-Airy beam & MPP

In contrast to Gaussian beams, ring-Airy beams combine controllable, long working distance, fairly stable and high aspect ratio focal volume, surpassing the restrictions set to the overall height of a 3D structure when using Gaussian beams and small working distance, high NA objective lenses. Compared Bessel beams which are the closest alternatives for fabricating long 3D structures, ring-airy beams are inferior in respect of the invariance of the voxel shape and focus accuracy. Bessel beams have already employed in DLW by MPP (ref 6,7).; Yang et al. showed microcylinder structures made by Bessel beams generated using a spatial light modulator while the height of the structure achieved was about 11 μm (ref. 7).

The ring-Airy beams provide controllable, long working distance and high aspect ratio focal volume, surpassing the restrictions set to the overall height of a 3D structure when using Gaussian beams and small working distance, high NA objective lenses. To demonstrate the capabilities of ring-airy beams for DLW by MPP we used them to fabricate 3D structures. Scanning Electron Microscope (SEM) images of hexagonal 3D structures fabricated using a ring-Airy beam, are shown in Figure 5.4 (a-d). Such structures could be useful as scaffolds for tissue engineering, as they provide the appropriate dimensions for cell growth [8, 10]. For the fabrication of these structures, the hybrid organic-inorganic, zirconium-propoxide doped photopolymerizable material was composed prepared as described in paragraph 5.3 [5].

The energy needed for the fabrication of these structures was 0,52 μJ . A schematic representation of the ring-Airy beam autofocuses into the volume of the photoresist droplet on a cover glass, is illustrated in Figure 5.1(b). Then, the sample is translated on the x-y plane, using linear stages, and the 3D structure is directly written. When the long ring-Airy focal voxel interacts with the photosensitive composite, a single illumination is enough in order a high aspect ratio photo-polymerizes column to form. From the SEM images (Figure 5.4 (c,d) we measured that the focal voxel has 2.8 μm diameter and 248 μm height. This results to an $\text{AR}=89\pm 20$. But due to the fact that the material sample was positioned about in the middle of the focus where the peak intensity is located, the real AR for a polymerized column is 132 ± 20 . The experimentally measured AR value is in good agreement with the estimated value from the intensity profiles (Fig. 4.9). Our results confirm that ring-Airy beams can fabricate really high and complete 3D structures by MPP.

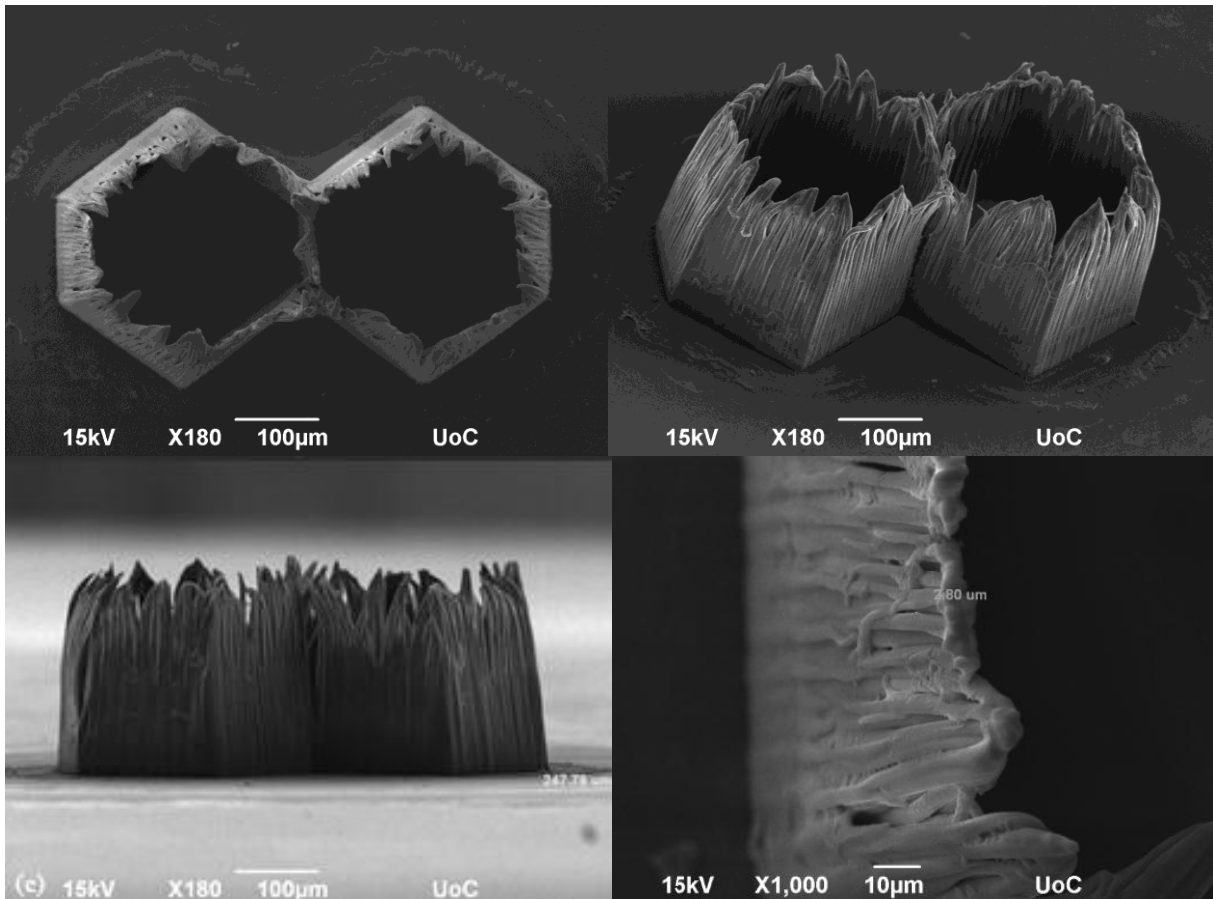


Figure 5.4| Fabricated 3D hexagonal structures using ring Airy beams: SEM images of hexagonal structures (250µm in height) made using ring Airy beams (a-d).

Therefore, ring-Airy beams can fabricate really high and complete 3D structures by MPP. Another, important issue here is the short time fabrication. Using Gaussian beams in DLW, the fabrication time of such large structure would be very time consuming; here a single laser shot is needed for each point of the structure, and the fabrication time is only limited by the speed of the translation stages.

These structures are a first representation of applying abruptly autofocusing beams for Multi-photon Polymerization. The height-limitation problem has been revealed using

ring-Airy beam due to the working distance controllable increase. The radially symmetric Airy beams proved to be an excellent choice for fabricating high structures by DLW that can be used for many significant applications like tissue engineering.

References

- 1 Fischer, J.; Wegener, M., Three-dimensional optical laser lithography beyond the diffraction limit. *Laser & Photonics Reviews* **2013**, *7*, 22-44.
- 2 Malinauskas, M.; Farsari, M.; Piskarkas, A.; Juodkazis, S., 3D structuring of transparent materials: a decade of advances. *Phys. Rep.* **2013**.
- 3 Buckmann, T.; Stenger, N.; Kadic, M.; Kaschke, J.; Frolich, A.; Kennerknecht, T.; Eberl, C.; Thiel, M.; Wegener, M., Tailored 3D Mechanical Metamaterials Made by Dip-in Direct-Laser-Writing Optical Lithography. *Advanced Materials* **2012**, *24*, 2710-2714.
- 4 Obata, K.; El-Tamer, A.; Koch, L.; Hinze, U.; Chichkov, B. N., High-aspect 3D two-photon polymerization structuring with widened objective working range (WOW-2PP). *Light-Science & Applications* **2013**, *2*.
- 5 Ovsianikov, A.; Viertl, J.; Chichkov, B.; Oubaha, M.; MacCraith, B.; Sakellari, I.; Giakoumaki, A.; Gray, D.; Vamvakaki, M.; Farsari, M.; Fotakis, C., Ultra-Low Shrinkage Hybrid Photosensitive Material for Two-Photon Polymerization Microfabrication. *ACS Nano* 2008, *2*, 2257-2262. J. Durnin, J.J. Miceli, J.H. Eberly, *Phys. Rev. Lett.* **58**, 1499 (1987)
- 6 B. Bhuian et al., Pattern generation using axicon lens beam shaping in two-photon polymerization, *Applied Surface Science*, 254, 841–844, (2007)
- 7 Liang Yang et al., Two-photon polymerization of cylinder microstructures by femtosecond Bessel beams *Appl. Phys. Lett.* 105, 041110 (2014)
- 8 V. Melissinaki, A. A. Gill, I. Ortega et al., “Direct laser writing of 3D scaffolds for neural tissue engineering applications,” *Biofabrication*, vol. 3, Article ID 045005, (2011)
- 9 Gabija Bickauskaite, MariaManousidaki et al, 3D Photonic Nanostructures via Diffusion-Assisted Direct fs LaserWriting, *Adv. in OptoElect.*, Article ID 927931, (2012)
- 10 M. Malinauskas, A. Zukauskas, K. Belazaras et al., “Laser fabrication of various polymer micro-optical components, *The European Physical Journal Applied Physics*, vol. 58, Article ID 20501, (2012)

In conclusion, the experimental generation of radially symmetric Airy beams by the Fourier Transform of a properly modulated Gaussian Laser beam, the study and control of their autofocusing characteristics and the use of these beams in Direct Laser writing technique by Multi-photon polymerization were the main parts of this Master thesis. We have shown that the focus position of abruptly autofocusing ring-Airy beams can be tailored, by pure optical means, to cover an extended range with almost invariant focal volume.

We demonstrate that the autofocusing position of a ring-Airy beam can be spatially controlled. These beams possess a high aspect ratio focal voxel that can be positioned at different working distances with almost invariant dimensions and shape. By adjusting the initial size of the primary Airy ring, its radius r_0 and width w , the manipulation of the focus position and magnitude is possible. Ring-Airy beams were used for long-range multiphoton polymerization. When a ring-Airy beam autofocuses within a photoresist, delivers high intensity contrast at the focal position and multiphoton absorption is directly induced. The controllable, long working distance and the high aspect ratio focal volume permit the direct fabrication of 3D microstructures (about 250 μm in height). As a result, the problem of short height structure is overcome by the use ring-Airy beams with controllable working distance. Also, we report on parametric results of such ring Airy beams and show that the working distance control of Bessel beams is obtainable too.

The use of radially symmetric autofocusing beams for Direct laser writing proved to be an excellent choice. We can modulate the structure's height by controlling the effective focal length of the ring-Airy beam according to the methods discussed before. In general, we increase the working distance of the optical system we want to use, and obtain it by modulating the characteristics of the ring-Airy that we employ. Moreover, the time consuming fabrication problem using Gaussian beams in DLW is solved by employing the abruptly autofocusing beams. Of course, there is still space of improvement, in order these beams to manage high resolution structures and may other structure geometries of various applications to be studied. Nevertheless, we believe that a new field of completely controllable beams to be used for tailored multiphoton polymerization, and not only, is opened.